Full determination of elastic scatterer characteristics from FFP measurements

Izar Azpiroz, Hélène Barucq, Julien Diaz, Rabia Djellouli

Full determination of elastic scatterer characteristics from FFP measurements

Izar Azpiroz, Hélène Barucq, Julien Diaz, Rabia Djellouli

RESEARCH REPORT

N° 9247

January 2019

Project-Team Magique-3D

ISSN 0249-6399 ISRN INRIA/RR--9247--FR+ENG

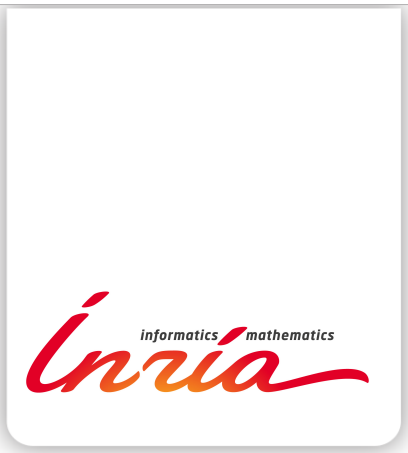

Full determination of elastic scatterer characteristics from FFP measurements

Izar Azpiroz *, Hélène Barucq*, Julien Diaz*, Rabia Djellouli†

Project-Team Magique-3D

Research Report n° 9247 — January 2019 — 69 pages

Abstract: A multi-stage computational strategy is proposed for determining all elastic scatterer characteristics including the shape, the material properties (Lamé coefficients and density), and the location from the knowledge of far-field pattern (FFP) measurements. The main feature of this new methodology is to utilize the well-known Tikhonov Newton algorithm in a multi-stage solution strategy. The adopted approach is critical for recognizing that the different nature and scales of the sought-after parameters as well as the frequency regime have different effect on the scattering observability. Numerical results obtained for illustrative two-dimensional elastic configurations highlight the performance of the designed solution methodology.

Key-words: Far-field pattern, elasto-acoustic scattering, Fréchet derivative

* Magique-3D,Inria E2S UPPA, Avenue de l'Université, BP 1155, 64013 PAU Cedex France, izar.azpiroz@inria.fr, helene.barucq@inria.fr, julien.diaz@inria.fr

† Department of Mathematics and Interdisciplinary Research Institute for the Sciences, IRIS College of Science and Mathematics, California State University, 18111 Nordhoff Street, Northridge, CA 91330, USA, rabia.djellouli@csun.edu

RESEARCH CENTRE
BORDEAUX – SUD-OUEST

200 avenue de la Vieille Tour
33405 Talence Cedex

Reconstruction complète des caractéristiques d'un obstacle élastique à partir de mesure en champ lointain

Résumé : Nous proposons une stratégie à plusieurs étapes pour déterminer toutes les caractéristiques physiques d'un diffracteur élastique à partir de mesures acoustiques en champ lointain. Ces caractéristiques sont la forme, les paramètres de matériau (coefficients de Lamé et densite), et la position. La principale caractéristique de cette nouvelle méthode est le couplage de l'algorithme de Tikhonov Newton avec une stratégie de résolution multi-étape. Cette approche est cruciale non seulement pour prendre en compte les différences de natures et d'échelles des paramètres à reconstruire mais également les effets des différents régimes de fréquence. Nous illustrons les performances de cette stratégie de résolution à l'aide de résultats numériques sur des configurations 2D.

Mots-clés : Champ lointain, diffraction élasto-acoustique, dérivée de Fréchet

Contents

Introduction

Inverse scattering problems, where information about an unknown object such as a body, or an inhomogeneity in a material, or a potential, is to be recovered from measurements of waves of fields scattered by this object, are fundamental for exploring objects that are not accessible to *in situ* measurements. This class of problems is notoriously very difficult to investigate mathematically and/or numerically [27]. The challenge is due to the fact that these problems are not only nonlinear but also ill-posed in the sense of Hadamard [38]. In spite of their difficulties, inverse scattering problems received a great deal of attention by mathematicians, scientists, and engineers, as attested by the prolificness of papers and conferences dedicated to this topic. This is due in part to their relevance to a wide range of important applications including seismology

[28, 35, 64, 16, 68], radar and sonar [53], optics [70], along with many other areas in science and medical imaging technology.

The inverse scattering problem considered in this paper consists in retrieving *all* the properties of an elastic scatterer from the knowledge of its far-field patterns (FFP) corresponding to one or multiple incident plane waves (see Section 2). To the best of our knowledge, this "full" inverse scattering problem has not been previously studied neither mathematically nor numerically. This work constitutes the first numerical attempt to simultaneously recover all the object properties: the shape of the scatterer, its material properties (the Lamé coefficients and the density), and its location. All existing numerical methods have been designed and so far employed for only partial parameters reconstruction. More specifically, extensive efforts have been devoted during the past five decades to the determination of the shape of an unknown object from the knowledge of its corresponding FFP measurements and the nature of the object. Indeed, various computational procedures have been designed for this purpose (see, e.g., [25, 32, 19, 42, 29, 30, 56, 57, 46, 22, 20, 21, 47, 61, 13], and the references therein). The problem of finding the material parameters (Lamé coefficients and density) of elastic scatterers has also been extensively studied and a wide range of numerical techniques have been developed to address it (see, e.g., [15, 72, 41, 54] and the references therein). Likewise, various numerical approaches have been proposed to locate objects from the knowledge of their corresponding FFP measurements and the nature of the objects, as reported in [3, 43, 33, 37, 73, 74], among other references. To conclude, reference [17] is the only paper that we encountered in the literature that proposes a technique to reconstruct simultaneously the shape of an object along with the two parameters that characterize the impedance boundary condition adopted in the considered mathematical model. We have not come across of any work that solves the inverse scattering problem considered in Section 2 and delivers the full characteristics of elastic scatterers from their FFP measurements.

Given that, our goal is to propose a solution methodology to fully recover the properties of an object from the knowledge of its corresponding FFP measurements. The proposed approach is a multi-stage strategy in which a regularized Newton algorithm plays a central role (see Section 3). The idea of using regularized Newton-type methods for solving inverse scattering problems is not new. The novelty here is that it is employed in a multi-stage context in order to recognize that the sought-after parameters (shape, material parameters, location) have, depending on the frequency regime, different influence on the scattering observability. The proposed strategy delivers first the shape and material parameters and then the scatterer's location is obtained in the second stage. Note that the scale variability of the parameters is addressed here via a rescaling procedure applied to the forward problems (see Section 1.3), whereas an appropriate choice of the regularization matrix addresses the sensitivity to the sought-after parameters' influence on the reconstruction (see Section 3.3).

The remainder of the paper is organized as follows. In Section 1, we specify the nomenclature and assumptions adopted in this paper, state the forward scattering problem, introduce the rescaling procedure employed to address the scale variability of the scatterer's parameters, and formulate the considered inverse scattering problem. Section 2 is devoted to the description of the designed solution methodology and its salient features. The main calculations required by the proposed inversion solver are described in Section 3. These are (a) the evaluation of the Jacobian matrix entries, (b) the solution of the forward problems that occur at each Newton iteration, and (c) the computation of the regularization matrix entries. A summary describing this new inversion algorithm along with its computational complexity are reported in Section 4. We present in Section 5 illustrative numerical parameters recovery for various scatterer's configurations including a disk, a non-convex octagon, and a mock-up submarine. The considered scatterers are made of steel and aluminum. These reconstructions have been performed using FFP measurements tainted with noise level ranging from 0% to 15%. The obtained results

highlight the performance efficiency of the proposed multi-stage solution methodology.

1 Preliminaries

We first describe the notations and the assumptions we adopt throughout this paper. We then describe the mathematical formulation of the elasto-acoustic scattering problem and its nondimensionalized version. Last, we state the considered inverse problem.

1.1 Nomenclature and Assumptions

Throughout this chapter, we adopt the following nomenclature and assumptions:

- Ω^s is a bounded domain of $\mathbb{R}^2$ representing an elastic obstacle.
- Ω^f is an infinite domain representing the fluid that surrounds Ω^s, i.e., $\Omega^f = \mathbb{R}^2 \setminus \overline{\Omega}^s$.
- Γ is the boundary of Ω^s and is assumed to be Lipschitz continuous.
- Σ is the exterior artificial boundary. Σ is a circle.
- $\boldsymbol{x} = (x_1, x_2)^T$ is a point of $\mathbb{R}^2$ and $r = \| \boldsymbol{x} \|_2$ is the distance from the origin point to $\boldsymbol{x}$ (in m).
- S^1 is the unit circle in $\mathbb{R}^2$, i.e., $S^1 = \{\boldsymbol{x} \in \mathbb{R}^2, \| \boldsymbol{x} \|_2 = 1\}$.
- ∇ (resp. Δ) is the gradient (resp. Laplace) operator in $\mathbb{R}^2$.
- ν is the outward normal to the boundaries Γ and Σ, and $\dfrac{\partial}{\partial \nu}$ is the normal derivative operator.
- k is a positive number representing the wavenumber of the incident plane wave (in m^{-1}) . $k = \dfrac{2\pi}{f c_f}$, where f is the frequency of the propagating wave (in Hz) and c_f is the sound speed in the fluid (in $\mathrm{m.s}^{-1}$).
- ω represents the angular frequency of the propagating wave (in $\mathrm{rad.s}^{-1}$). $\omega = 2\pi f$.
- $\boldsymbol{d} \in S^1$ is a unit vector representing the direction of the incident plane wave.
- λ and μ are two positive numbers representing the Lamé coefficients of the considered elastic object Ω^s (in Pa).
- ρ_s is a positive number representing the density of the elastic obstacle Ω^s (in $\mathrm{kg.m}^{-3}$).
- M^* denotes the adjoint matrix of M. M^* is the complex conjugate of the transpose matrix of M, i.e, $M^* = \overline{M}^t$.

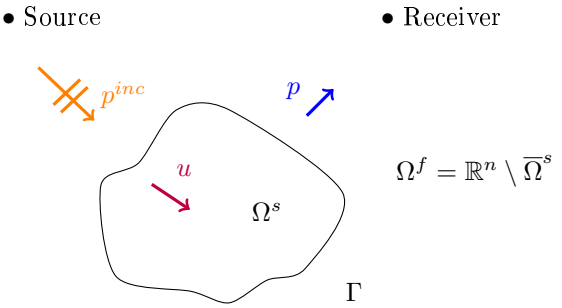

Figure 1: Schematic description of the problem statement.

1.2 Mathematical Formulation of the Problem

The scattering of time-harmonic acoustic waves by an elastic obstacle Ω^s embedded in an infinite homogeneous medium Ω^f (see Fig. 1) can be formulated as the following boundary value problem (BVP):

$$(BVP)\begin{cases} \nabla\cdot\sigma(u)+\omega^2\rho_s u=0 & \text{in } \Omega^s \quad \text{(a)}\\ \Delta p+k^2 p=0 & \text{in } \Omega^f \quad \text{(b)}\\ \sigma(u)\cdot\nu=-p\nu-g\nu & \text{on } \Gamma \quad \text{(c)}\\ \omega^2\rho_f u\cdot\nu=\frac{\partial p}{\partial\nu}+\frac{\partial g}{\partial\nu} & \text{on } \Gamma \quad \text{(d)}\\ \lim\limits_{r\to+\infty}\sqrt{r}\left(\frac{\partial p}{\partial r}-ikp\right)=0 & \text{(e)} \end{cases} \tag{1}$$

where the pair (u,p) represents the elasto-acoustic scattered field vector; p is the scalar-valued fluid pressure in Ω^f, and $u=(u_x,u_y)^t$ is the vector-valued displacement field in Ω^s; $g=p^{inc}=e^{i\omega/c_f\boldsymbol{x}\cdot\boldsymbol{d}}$ corresponds to the given incident plane wave. The stress tensor σ is related to the strain tensor ϵ by Hooke's law [45]. Note that this study is limited to the case of an isotropic medium, so that the stiffness tensor is invariant under rotations and reflections [45]. Consequently, we have

$$\sigma(u)=\lambda\nabla\cdot u\boldsymbol{I}\ +\ 2\mu\epsilon(u), \tag{2}$$

where ϵ is the strain tensor given by

$$\epsilon(u)=\frac{1}{2}\left(\nabla u\ +(\nabla u)^T\right). \tag{3}$$

Hence, Ω^s is assumed to be a homogeneous scatterer. Observe that the direct problem BVP (1) contains the standard exterior Helmholtz problem given by equations (b) and (e), and the Navier equation given by (a) governing the equilibrium of an elastic scatterer. These equations are coupled via the transmission conditions given by (c) and (d). The first one is a dynamic interface condition whereas the second one is a kinematic interface condition [45]. Furthermore, p_∞, the far-field pattern (FFP) corresponding to the scattered pressure field p, can be expressed

using the following integral representation [27]:

$$p_\infty(\hat{\boldsymbol{x}}) = \frac{e^{i\pi/4}}{\sqrt{8\pi k}} \int_\Gamma \left(e^{-ik\hat{\boldsymbol{x}}\cdot\boldsymbol{y}} \frac{\partial p}{\partial \nu}(\boldsymbol{y}) - \frac{\partial e^{-ik\hat{\boldsymbol{x}}\cdot\boldsymbol{y}}}{\partial \nu} p(\boldsymbol{y}) \right) dX; \quad \hat{\boldsymbol{x}} \in S^1. \tag{4}$$

Note that BVP has been extensively studied. Mathematical results pertaining to existence, uniqueness, and regularity of the solution can be found in [45, 10, 40, 7, 12, 63], among other references.

1.3 Nondimensionalization of the Forward Problem

The characteristic parameters of a given elastic scatterer Ω^s are of different *nature*. Indeed, it has been reported in [6, 7] that the sensitivity of the FFP given by (4) to changes on the shape Γ is in general quite different to the ones on the material parameters λ, μ, and ρ_s. Such a variability can have, depending on the frequency regime, a dramatic impact on the scattering observability. Furthermore, the magnitude of these parameters is also different. For example, in the numerical experiments reported in Section 5, the Lamé coefficients λ and μ are of order 1GPa, the density is of order 10^4kg m^{-3}, whereas the size of the obstacle is of order 10^{-3}m. Such a difference constitutes a serious numerical challenge when attempting to simultaneously recover these parameters from FFP measurements. Given that, there is undoubtedly a real advantage in *rescaling* the forward problem prior to solving the inverse obstacle problem introduced in Section 1.4. To this end, we proceed in a classical way by rescaling each of the parameters in BVP 1) by a characteristic unit of measure to be determined. Specifically, we introduce the following notation:

$$\hat{v} = \frac{v}{v_0} \tag{5}$$

where v represents one of the parameters $\omega, c_f, \rho_s, \lambda, \mu, u_x, u_y, p$ and v_0 is a characteristic unit of measure v to be determined. In addition, we use a dilation factor L for the position coordinates $\boldsymbol{x} = (x, y)$, i.e., $\hat{\boldsymbol{x}} = \frac{1}{L}\boldsymbol{x}$. Furthermore, we assume that $u_{x,0} = u_{y,0} = u_0$. We then rewrite BVP(1) in terms of the new dimensionless quantities $\hat{v}$. We also set all the arising constants to be 1, i.e.,

$$\frac{C_0}{x_0^2\omega_0^2\rho_{s,0}} = \frac{c_{f,0}^2}{L^2\omega_0^2} = \frac{\omega_0^2 u_0 \rho_{s,0} L}{p_0} = \frac{C_0 u_0}{L p_0} = \frac{\omega_0 L}{c_{f,0}} = 1. \tag{6}$$

In doing so, we deduce that $(\hat{u}, \hat{p})$ also satisfies BVP(1) but with dimensionless quantities. Last, we must point out that in all numerical experiments reported in Section 5, we have selected:

- $p_0 = 1$Pa.
- ω_0 is the angular frequency in each considered numerical experiment.
- $L = L^{(0)}$, where $L^{(0)}$ is the characteristic size of the initial obstacle $\Omega^{s\,(0)}$.
- $C_0 = \lambda^{(0)} + 2\mu^{(0)}$, where $\lambda^{(0)}$ and $\mu^{(0)}$ are the Lamé coefficients of the initial obstacle $\Omega^{s\,(0)}$.

The values of the remaining quantities $\rho_{s,0}, c_{f,0}, u_0$ are then deduced from the relations given by (6).

1.4 The Inverse Problem Formulation

As stated in the Introduction section, the main goal of this work is to fully characterize elastic scatterers from the knowledge of some corresponding FFP measurements. Therefore, we consider the following inverse obstacle problem (IOP):

Given one or several measured far field patterns $\widetilde{p_\infty}(\hat{\boldsymbol{x}})$ *corresponding to one or several given directions* $\boldsymbol{d}$ *and wavenumbers* k *of incident plane waves, find* Γ *the shape of the scatterer* Ω^s*, its Lamé coefficients* (λ, μ)*, its density* ρ_s*, and its location* $\boldsymbol{x_c}$ *such that*

$$F\left(\Gamma, \lambda, \mu, \rho_s, \boldsymbol{x_c}\right)(\hat{\boldsymbol{x}}) = \widetilde{p_\infty}(\hat{\boldsymbol{x}}); \quad \hat{\boldsymbol{x}} \in S \subseteq S^1 \tag{7}$$

where F *is the far-field operator that maps* $(\Gamma, \lambda, \mu, \rho_s, \boldsymbol{x_c})$ *onto the far-field pattern* $\widetilde{p_\infty}$*. The tilde notation designates a measured quantity, i.e., a quantity that can be tainted with errors during the measurement process.*

To the best of our knowledge, there were no attempts, reported in the literature, to investigate IOP (7), either mathematically or numerically. It is worth noting however that in the case of a rigid obstacle, i.e., Γ being the only unknown in IOP(7), in addition to an extensive numerical investigation (see, e.g.,[27, 25, 55, 50, 32, 42, 26]), various results pertaining to the uniqueness have been established and can be found in [27, 42, 51, 44], among other references.

2 The Proposed Multi-Stage Solution Methodology

As stated earlier in the Introduction section, the main goal of this study is to propose an efficient computational procedure for solving IOP(7). The method we have designed is a multi-stage strategy in which a regularized Newton algorithm plays a central role. The multi-stage feature of the method is adopted to recognize that the shape, the material parameters, and the location of the sought-after elastic object along with the frequency regime have different effects on the acoustic scattering observability. More specifically:

- The shape of the scatterer and its material properties are of different nature and scales. Their variations have different influence on the FFP, as reported in [6, 7]. Hence, the proposed approach addresses the *scale* issue by considering the non dimensional formulation (see Section 1.3) when solving the forward scattering-type problems that occur at each Newton iteration. Furthermore, the different *nature* issue is addressed through the Tikhonov regularization procedure. Indeed, when retrieving simultaneously the shape and the material parameters, the proposed method uses different sets of regularization parameter values, as detailed in Section 3.3.

- It is well-known that, in general, Newton methods cannot determine the location of the sought-after object from the knowledge of the FFP intensity. This is due to the fact that the FFP intensity is invariant under translation of the scatterer [44, 27]. On the other hand, it is also well-known that, in practice, the measurements of the FFP intensity are more accurate than the measurements of the phase of the FFP. Hence, since accurate data are very important to ill-posed problems, the proposed method employs the FFP intensity measurements to first recover the shape and the material parameters while keeping the location of the sought-after obstacle "frozen" at the origin of the plane. Once this stage is completed, the proposed algorithm uses the FFP measurements to locate the scatterer.

Next, we examine the algorithmic and computational considerations of the proposed solution methodology and report on its performance when applied to retrieving the parameters of various two-dimensional elastic objects including a disk, a non convex octagon, and a mockup submarine.

2.1 The Regularized Newton Method

Regularized iterative methods have been among the primary candidates since the mid-80s for solving both two -and three- dimensional scattering problems (see, e.g., [32, 50, 55, 62, 60, 67, 71, 48, 49, 34, 4, 52]). The Newton iterative aspect of these methods addresses effectively the nonlinearity of the IOPs whereas the regularization component is incorporated to restore the stability, as defined by Hadamard in [38]. In what follows, we recall the main features of the regularized Newton method that we employ in the context of the proposed multi-stage solution methodology.

2.1.1 The parametrization.

We assume that the sought-after fluid-structure interface Γ can be parametrized as follows:

$$\Gamma = \Gamma(\boldsymbol{s}) \quad ; \quad \boldsymbol{s} = [s_1, ..., s_{N_{\boldsymbol{s}}}]^T \in \mathbb{R}^{N_{\boldsymbol{s}}} \tag{8}$$

where $N_{\boldsymbol{s}}$ denotes the total number of shape parameters $\boldsymbol{s_j}$. The choice of the parameters depends on the *a priori* knowledge on the shape of the scatterer [32, 27]. We set

$$\boldsymbol{q} = \left[\boldsymbol{s}^T, \lambda, \mu, \rho_s, \boldsymbol{x_c}\right]^T \in \mathbb{R}^{N_{\boldsymbol{q}}} \tag{9}$$

where $\boldsymbol{x_c} = (x_c, y_c)$ represents the location of the sought-after scatterer. $N_{\boldsymbol{q}}$ is the total number of unknown parameters of IOP (7). Hence, $N_{\boldsymbol{q}} = N_{\boldsymbol{s}} + 5$.

Since the far-field pattern p_∞ of the scattered pressure field p is measured at a finite number of given points $\hat{\boldsymbol{x}}_{\boldsymbol{j}} \in S^1$, denoted by $N_{\hat{\boldsymbol{x}}}$, we project IOP (7) onto a finite dimensional space of $L^2(S^1)$, which is the natural choice for the measurements' space, and transform it onto the following algebraic problem:

$$\begin{cases} \text{Find } \boldsymbol{q} \in \mathbb{R}^{N_{\boldsymbol{q}}} \text{ such that} \\ F\left(\boldsymbol{q}\right)\left(\hat{\boldsymbol{x}}_{\boldsymbol{j}}\right) = \widetilde{p_\infty}(\hat{\boldsymbol{x}}_{\boldsymbol{j}}); \quad j = 1, ..., N_{\hat{\boldsymbol{x}}} \end{cases} \tag{10}$$

Observe that the resulting inverse problem given by (10) is a discrete formulation of IOP (7). It is a nonlinear algebraic system with $N_{\hat{\boldsymbol{x}}}$ equations and $N_{\boldsymbol{q}}$ unknowns; $N_{\hat{\boldsymbol{x}}}$ being larger than $N_{\boldsymbol{q}}$ when reconstructing with full aperture measurements.

2.1.2 The regularized Newton equation using the full data (FFP).

The solution of the nonlinear inverse problem IOP (10) by the Newton method incurs, at each Newton iteration n, the solution of the following linear algebraic system:

$$J_F\left(\boldsymbol{q}^{(n)}\right)\left(\hat{\boldsymbol{x}}_{\boldsymbol{j}}\right)\boldsymbol{\delta q}^{(n)} = \widetilde{p_\infty}(\hat{\boldsymbol{x}}_{\boldsymbol{j}}) - p_\infty^{(n)}\left(\hat{\boldsymbol{x}}_{\boldsymbol{j}}\right); \qquad j = 1, ..., N_{\hat{\boldsymbol{x}}} \tag{11}$$

where

- $J_F\left(\boldsymbol{q}^{(n)}\right)$ is the $N_{\hat{\boldsymbol{x}}} \times N_{\boldsymbol{q}}$ Jacobian matrix of the operator F. $J_F\left(\boldsymbol{q}^{(n)}\right)\left(\hat{\boldsymbol{x}}_{\boldsymbol{l}}\right)$ is the l^{th} row vector whose entries are the Fréchet derivatives of the far-field pattern with respect to the vector parameter coordinates $\boldsymbol{q}$.

- $p_\infty^{(n)}(\hat{\boldsymbol{x}}_{\boldsymbol{l}}) = F\left(\boldsymbol{q}^{(n)}\right)(\hat{\boldsymbol{x}}_{\boldsymbol{l}})$ is the far-field pattern corresponding to the computed configuration $\Omega^{s(n)}$ at iteration n.

Once the vector $\boldsymbol{\delta q}^{(n)} \in \mathbb{R}^{N_{\boldsymbol{q}}}$ is calculated, the value of the sought-after parameter vector is then updated as follows:

$$\boldsymbol{q}^{(n+1)} = \boldsymbol{q}^{(n)} + \boldsymbol{\delta q}^{(n)} \tag{12}$$

Moreover, since in practice the number of observation points $N_{\hat{x}}$ is greater than the number of the parameters $N_{\boldsymbol{q}}$, the linear system (11) is overdetermined. Therefore, it is solved in the least-squares sense. Hence, the linear system given by (11) is replaced by the following corresponding *normal* equations:

$$J_F^*\left(\boldsymbol{q}^{(n)}\right) J_F\left(\boldsymbol{q}^{(n)}\right) \boldsymbol{\delta q}^{(n)} = J_F^*\left(\boldsymbol{q}^{(n)}\right)\left(\widetilde{\boldsymbol{p_\infty}} - \boldsymbol{p_\infty}^{(n)}\right) \tag{13}$$

where

- $\widetilde{p_\infty}$ is the FFP measurements vector, that is,

$$\widetilde{\boldsymbol{p_\infty}} = [\widetilde{p_\infty}(\hat{\boldsymbol{x}}_{\boldsymbol{1}}), ..., \widetilde{p_\infty}(\hat{\boldsymbol{x}}_{\boldsymbol{N_{\hat{x}}}})]^T$$

- $\boldsymbol{p}_{\boldsymbol{\infty}}^{(n)}$ is the FFP computed vector at iteration n, that is,

$$\boldsymbol{p}_{\boldsymbol{\infty}}^{(n)} = \left[p_\infty^{(n)}(\hat{\boldsymbol{x}}_{\boldsymbol{1}}), ..., p_\infty^{(n)}(\hat{\boldsymbol{x}}_{\boldsymbol{N_{\hat{x}}}})\right]^T.$$

Due to the ill-posedness nature of IOP (7), the discrete linear system (13) is severely ill-conditioned. This means that small perturbations in the data may lead to large changes in the solution. For this reason, a regularization procedure must be incorporated into (13) to address the lack of stability [31, 36]. We propose a Tikhonov-based strategy to restore the stability to the linear system (13) [66, 65]. This consists in replacing (13) by the following *regularized* system:

$$\left(J_F^*\left(\boldsymbol{q}^{(n)}\right) J_F\left(\boldsymbol{q}^{(n)}\right) + \mathfrak{R}^{(n)}\right) \boldsymbol{\delta q}^{(n)} = J_F^*\left(\boldsymbol{q}^{(n)}\right)\left(\widetilde{\boldsymbol{p_\infty}} - \boldsymbol{p_\infty}^{(n)}\right) \tag{14}$$

where $\mathfrak{R}^{(n)}$ is a $N_{\boldsymbol{q}} \times N_{\boldsymbol{q}}$ *diagonal* and definite positive matrix, called the regularization matrix. The selection of the diagonal entries of $\mathfrak{R}^{(n)}$ is discussed in Section 3.3.

2.1.3 The regularized Newton equation using the reduced data (FFP intensity).

It is well-known that in practice the FFP intensity measurements are obtained with higher accuracy level than the corresponding phase measurements. In addition, accurate data are very important to ill-posed problems. Therefore, we propose to use the *intensity* of the measured far-field pattern when retrieving the parameters $\boldsymbol{s}, \lambda, \mu$, and ρ_s. Note that the intensity of the FFP is defined here as the *square* of the amplitude of the FFP:

$$U\left(\boldsymbol{q}^{(n)}\right)(\hat{\boldsymbol{x}}_{\boldsymbol{j}}) = \overline{F\left(\boldsymbol{q}^{(n)}\right)(\hat{\boldsymbol{x}}_{\boldsymbol{j}})} F\left(\boldsymbol{q}^{(n)}\right)(\hat{\boldsymbol{x}}_{\boldsymbol{j}}) = \mid \boldsymbol{p_\infty}^{(n)}(\hat{\boldsymbol{x}}_{\boldsymbol{j}}) \mid^2; \quad j = 1, ..., N_{\hat{x}}$$

Consequently, the computation of the vector $\boldsymbol{\delta q}^{(n)}$ needed in (12) is obtained by solving the following regularized least-squares systems:

$$\left(J_U^*\left(\boldsymbol{q}^{(n)}\right) J_U\left(\boldsymbol{q}^{(n)}\right) + \mathfrak{R}^{(n)}\right) \boldsymbol{\delta q}^{(n)} = J_U^*\left(\boldsymbol{q}^{(n)}\right)\left(\widetilde{\boldsymbol{U}} - \boldsymbol{U}\left(\boldsymbol{q}^{(n)}\right)\right) \tag{15}$$

where $J_U\left(\boldsymbol{q}^{(n)}\right)$ is the Jacobian matrix corresponding to the intensity operator $\boldsymbol{U}\left(\boldsymbol{q}^{(n)}\right)$. It is given by:

$$J_U\left(\boldsymbol{q}^{(n)}\right) = 2\mathcal{R}e\left[\overline{F(\boldsymbol{q}^{(n)})}^T J_F(\boldsymbol{q}^{(n)})\right] \tag{16}$$

when $\mathcal{R}e$ designates the real part of a complex valued quantity and $\widetilde{\boldsymbol{U}}$ denotes the measured intensity vector. It is defined by:

$$\widetilde{\boldsymbol{U}} = \left[|\, \widetilde{\boldsymbol{p_\infty}}(\hat{\boldsymbol{x}}_{\mathbf{1}})\,|^2, ..., |\, \widetilde{\boldsymbol{p_\infty}}(\hat{\boldsymbol{x}}_{\boldsymbol{N_{\hat{x}}}})\,|^2\right]^T$$

Similarly, $U\left(\boldsymbol{q}^{(n)}\right)$ denotes the computed intensity vector at iteration n. It is given by:

$$\boldsymbol{U}\left(\boldsymbol{q}^{(n)}\right) = \left[U\left(\boldsymbol{q}^{(n)}\right)(\hat{\boldsymbol{x}}_{\mathbf{1}}), ..., U\left(\boldsymbol{q}^{(n)}\right)(\hat{\boldsymbol{x}}_{\boldsymbol{N_{\hat{x}}}})\right]^T.$$

We must point out that it is not possible in general to retrieve the location $\boldsymbol{x_c}$ of the sought-after scatterer from the knowledge of its corresponding FFP intensity. This is due to the fact that the FFP intensity operator is *invariant* under translations of the scatterer Ω^s (see, e.g., [27, 44, 43] or Appendix D, pp. 207–208 in [6]). For this reason, the linear system (15) will be employed to recover the shape and the material parameters of Ω^s only.

2.2 The Multi-Stage Solution Procedure

The proposed solution method is a multi-stage procedure in which the regularized Newton algorithm given by (14)-(12) or (15)-(12) is its corner stone. The proposed method recognizes that the sought-after parameters have different influence on the scattering observability and can be described as follows:

Stage 0. We initiate the algorithm by selecting an arbitrary value of the initial vector parameter $\boldsymbol{q}^{(0)}$.

Stage 1. This stage is devoted to the simultaneous recovery of the shape and material parameters $\left[\boldsymbol{s}^T, \lambda, \mu, \rho_s\right]^T$. This is accomplished by iterating the regularized Newton system (15) and (12).

Stage 2. This stage is dedicated to the determination of the location $\boldsymbol{x_c}$ of the elastic scatterer computed in Stage 1. This goal is achieved by iterating the regularized Newton system (14) and (12).

3 The Computational Requirements

We describe in this section the three critical steps of the algorithm: the evaluation of the Jacobians, the solution of the forward problem, and the computation of the regularization matrix.

3.1 Effective Evaluation of the Jacobians

As indicated in (14) and (15), a key step for employing the proposed regularized Newton algorithm is the computation, at each Newton iteration n, of the $N_{\hat{x}} \times N_{\boldsymbol{q}}$ entries of the Jacobian matrix $J_F(\boldsymbol{q}^{(n)})$. Such calculations must be performed efficiently and with a high accuracy level to ensure stability, fast convergence, and cost effectiveness of the proposed computational procedure. To do this, we exploit the mathematical results pertaining to the dependence of the

operator F with respect to the domain [11, 12] and to the material parameters [6, 7]. The results established in [11] state that the operator F is continuously differentiable with respect to the domain Ω^s. This result has been established assuming the domain Ω^s to be Lipschitz continuous. Moreover, the result reported in [12] provides a characterization of the derivative of F with respect to the boundary of Ω^s, that is of practical computational interest. The proof of the result assumes Ω^s to be a Lipschitz continuous polygonal domain. Furthermore, the results established in [6, 7] prove that F is also continuous differentiable with respect to the material parameters and provide a characterization of its corresponding derivatives. More specifically, let $p_l^{\prime(n)}$ (resp. $u_l^{\prime(n)}$) be the derivative of the pressure field p (resp. displacement field u) in the direction of a considered parameter q_l; $l = 1, ..., N_{\boldsymbol{q}}$ at iteration n, i.e., corresponding to the configuration $\Omega^s(\boldsymbol{q}^{(n)})$. Then, the pair $(p_l^{\prime(n)}, u_l^{\prime(n)})$ is the solution of the following elasto-acoustic scattering-type problem:

$$
(BVP) \left\{ \begin{array}{rcll}
\nabla \cdot \sigma(u_l^{\prime(n)}) + \omega^2 \rho_s u_l^{\prime(n)} = & f_1^{(n)} & \text{in } \Omega^{s(n)} & \text{(a)} \\
\Delta p_l^{\prime(n)} + k^2 p_l^{\prime(n)} = & f_2^{(n)} & \text{in } \Omega_b^{f(n)} & \text{(b)} \\
\sigma(u_l^{\prime(n)}) \cdot \nu + p_l^{\prime(n)} \nu = & g_1^{(n)} & \text{on } \Gamma^{(n)} & \text{(c)} \\
\omega^2 \rho_f u_l^{\prime(n)} \cdot \nu - \frac{\partial p_l^{\prime(n)}}{\partial \nu} = & g_2^{(n)} & \text{on } \Gamma^{(n)} & \text{(d)} \\
\lim\limits_{r \to +\infty} \sqrt{r} \left(\frac{\partial p_l^{\prime(n)}}{\partial r} - ikp_l^{\prime(n)} \right) = & 0 & & \text{(e)}
\end{array} \right. \tag{17}
$$

where $f_1^{(n)}, f_2^{(n)}, g_1^{(n)}$ and $g_2^{(n)}$ are functions whose expressions depend on the nature of the parameter q_l. More specifically:

- If q_l is a shape or a position parameter, then $f_1^{(n)} = f_2^{(n)} = 0$ and :

$$g_1^{(n)} = -h_j^t \nabla \sigma(u^{(n)}) \nu - \nabla (p^{(n)T} \cdot h_j^{(n)} \nu + \sigma(u^{(n)}) [h_j']^t \nu + (p^{(n)T} [h_j']^t \nu;$$

$$g_2^{(n)} = -(\omega^2 \rho_f \nabla u^{(n)} - \nabla(\nabla(p^{(n)T})) h_j \cdot \nu + (\omega^2 \rho_f u^{(n)} - \nabla(p^{(n)T}) \cdot [h_j']^t \nu.$$

  where

$$h_l^{(n)} = \frac{\partial \Gamma}{\partial q_l}(\boldsymbol{q}^{(n)}). \tag{18}$$

- If q_l is the Lamé coefficient λ, then $f_2^{(n)} = g_2^{(n)} = 0$ and we have:

$$f_1^{(n)} = -\nabla \cdot \left(\nabla \cdot u^{(n)} \boldsymbol{I} \right); \tag{19}$$

$$g_1^{(n)} = -\left(\nabla \cdot u^{(n)} \boldsymbol{I} \right) \cdot \nu. \tag{20}$$

- If q_l is the Lamé coefficient μ, then $f_2^{(n)} = g_2^{(n)} = 0$ and we have:

$$f_1^{(n)} = -2 \nabla \cdot \epsilon(u^{(n)}); \tag{21}$$

$$g_1^{(n)} = -2 \epsilon(u^{(n)}) \cdot \nu. \tag{22}$$

- If q_l is the density coefficient ρ, then $f_2^{(n)} = 0$; $g_1^{(n)} = g_2^{(n)} = 0$ and we have:

$$f_1^{(n)} = -\omega^2 u^{(n)}. \tag{23}$$

Once the derivatives $p_l'^{(n)}$ and $u_l'^{(n)}$ are evaluated, the "far-field pattern" $p_{l,\infty}'^{(n)}$, at iteration n, is then post-processed using the integral representation given by (4) with $p_l'^{(n)}$ and $\Gamma^{(n)}$. Consequently, we deduce the entries of the Jacobian matrix $J_F(\boldsymbol{q}^{(n)})$ as follows:

$$J_F(\boldsymbol{q}^{(n)})_{lj} = p_{l,\infty}'^{(n)}(\hat{x}_j) \quad j = 1, ..., N_{\hat{x}}; \quad l = 1, ..., N_{\boldsymbol{q}}. \tag{24}$$

Hence, it follows that, at each regularized Newton iteration n, the Jacobian matrix $J_F(\boldsymbol{q}^{(n)})$ can be computed by solving $N_{\boldsymbol{q}}$ direct elasto-acoustic scattering-type problems that differ only by additional terms in the transmission conditions and/or in the wave equations. This means that, at the algebraic level (that results from any finite element-type discretization [24]), the matrix entries of $J_F(\boldsymbol{q}^{(n)})$ are obtained by solving a single linear system with multiple right-hand sides.

3.2 Solving Efficiently the Forward Problem

At each iteration n, the regularized Newton system (see (14) and (15)) calls for the solution of the elasto-acoustic scattering problem BVP(1) and BVP(17). Although these problems are linear in nature, their numerical solutions are notoriously difficult due mainly to the following two reasons: (a) they are set in an unbounded (infinite) domain, and (b) the scattered field is highly oscillatory (for high frequency regime).

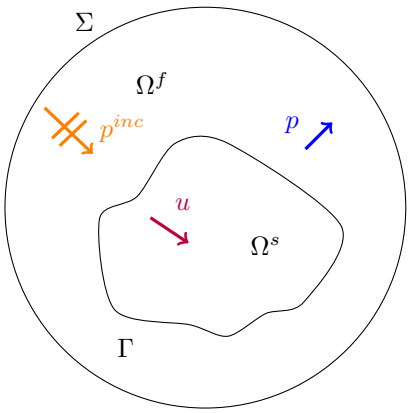

Figure 2: Schematic description of the problem statement in a finite domain.

To address the unboundness aspect of the problem, we propose to reformulate BVP(1) and BVP(17) in a bounded domain Ω_Σ^f, by surrounding the scatterer Ω^s with an artificial boundary Σ (see Fig. 2). The Sommerfeld condition (see (e) of BVP(1) and BVP(17)) is then replaced by the following exterior boundary condition of first order, in the sense of the pseudo-differential framework adopted in [5]:

$$\frac{\partial p}{\partial \nu} = ikp - \frac{\kappa}{2}p \qquad \text{on } \Sigma. \tag{25}$$

where κ denotes the curvature of Σ. Since we have chosen Σ to be a circle of radius R, then $\kappa = \frac{1}{R}$. We have chosen this Robin-type boundary conditions for mainly the following two considerations: (a) its computational simplicity and (b) its performance efficiency. Indeed, the approximation of the boundary condition (25) by a finite element method introduces only additional mass-like matrices defined on the exterior boundary Σ. Building these matrices is straightforward. Moreover, when compared to a second-order absorbing boundary condition [14] or to a perfectly matched layer (PML) condition [23], it has been reported in [8] that the first-order absorbing boundary condition (25) exhibits a comparable accuracy level, if not better, when employed in the low- and mid- frequency regime, i.e., the frequency band considered in this paper. Needless to say that one may use higher order absorbing boundary condition when performing these calculations in high frequency regime.
Once the direct scattering problems BVP (1) and BVP (17) are formulated in a bounded domain Ω_Σ^f, we solve them numerically using the interior penalty discontinuous Galerkin (IPDG) method introduced in [9]. The proposed IPDG method possesses two distinctive features. First, it employs high-order polynomial functions to ensure an accurate approximation of highly oscillating waves. Second, it is equipped with curved boundary edges to provide an accurate representation of the fluid-structure interface Γ. The importance of an accurate representation of Γ has been demonstrated by the numerical results reported in [9]. These results indicate that (a) there is an improvement on the accuracy level by -at least- two orders of magnitude and (b) unlike when approximating Γ by a "broken" line, there are no more spurious internal resonances in the fluid region.
The IPDG formulation can be expressed, at the algebraic level, as follows [9]:

$$\begin{pmatrix} \boldsymbol{A^f} + \boldsymbol{C} & \boldsymbol{B} \\ \boldsymbol{B^*} & \boldsymbol{A^s} \end{pmatrix} \begin{pmatrix} P \\ U \end{pmatrix} = \begin{pmatrix} F_1 \\ F_2 \end{pmatrix} \tag{26}$$

where $\boldsymbol{A^f}$ (resp. $\boldsymbol{A^s}$) is a symmetric matrix given by:

$$\boldsymbol{A^f} = \frac{1}{\omega^2}(\boldsymbol{K^f} - k^2\,\boldsymbol{M^f} - \boldsymbol{J^f} + \boldsymbol{S^f}), \tag{27}$$

resp.

$$\boldsymbol{A^s} = \boldsymbol{K^s} - \omega^2\rho_s\,\boldsymbol{M^s} - \boldsymbol{J^s} + \boldsymbol{S^s}, \tag{28}$$

where

- $\boldsymbol{K^f}$ (resp. $\boldsymbol{K^s}$) is a block diagonal stiffness matrix associated to the pressure (resp. the displacement) field.
- $\boldsymbol{M^f}$ (resp. $\boldsymbol{M^s}$) is a block diagonal mass matrix associated to the pressure (resp. the displacement) field.
- $\boldsymbol{J^f}$ (resp. $\boldsymbol{J^s}$) is a matrix that contains the jump terms. The entries of this matrix are defined over the interior edges in the fluid (resp. in the solid).
- $\boldsymbol{S^f}$ (resp. $\boldsymbol{S^s}$) is a mass-like matrix defined over the interior edges in the fluid (resp. in the solid) resulting from the penalty term.

$\boldsymbol{C}$ is the complex-valued damping matrix. It is a mass-like matrix, whose entries are all zeros except for the elements located at the exterior boundary Σ. The matrix $\boldsymbol{A^f} + \boldsymbol{C}$ is symmetric, but non-hermitian, and thus not positive-definite.

Note that the matrix $\boldsymbol{A^s}$ is positive-definite up to the Jones frequencies [63, 10]. Note that the interior penalty term compensates the weak ellipticity of the equation operator. $\boldsymbol{B}$ is a mass-like boundary matrix whose entries are defined on the interface edges only, whereas F_1 and F_2 are the source vectors. The vector P (resp. U) is the fluid pressure (resp. structural displacement) representation in the finite element basis.

The linear system given by (26) is thus composed of sparse matrices whose symmetry property allows for an optimized storage. This system is solved with the LU factorization procedure developed for sparse systems and incorporated in the open-source program suite, MUMPS [1, 2]. Note that in the low- and mid- frequency regimes, the sparse implementation allows running the numerical experiments on a personal computer.

Last, as shown is Section 3.1, the Fréchet derivative of the elasto-acoustic scattered field with respect to the parameter q_j can be evaluated at each iteration by solving the same system of equations but with different right-hand sides. Then, the corresponding far-field pattern, that is the Fréchet derivative of the FFP with respect to q_j, is obtained by post-processing the solution using the integral representation given by (4) on the boundary $\Gamma^{(n)}$.

3.3 Computation of the regularization matrix $\mathfrak{R}^{(n)}$

It is well-known that the convergence of any regularized iterative algorithm strongly depends on the effectiveness of its regularization procedure. For this reason, various strategies have been developed for selecting "optimal" regularization values [58, 59, 69, 39]. However, all these strategies have been designed based on theoretical considerations that unfortunately are limited to linear problems. Given that, we propose to employ a trial and error strategy for selecting, at each Newton iteration, the diagonal entries of the regularization matrix $\mathfrak{R}^{(n)}$. Such a choice is a balance act between the stability of the algorithm and its accuracy. Note that the proposed "brute force" approach recognizes the different influences of the sought-after parameters on the scattering observability. This is why the choice of the entries of $\mathfrak{R}^{(n)}$ depends on the algorithm stage.

In what follows, we describe how to select the regularization matrix $\mathfrak{R}^{(n)}$ in each stage of the proposed iterative algorithm.

3.3.1 The choice of $\mathfrak{R}^{(n)}$ in Stage I.

We first recall that Stage I is dedicated to the simultaneous search of the shape parameter vector $\boldsymbol{s} \in \mathbb{R}^{N_{\boldsymbol{s}}}$ and the material parameter triplet $(\lambda, \mu, \rho_s) \in \mathbb{R}^3$. Therefore, the regularization matrix $\mathfrak{R}^{(n)}$ is a $(N_{\boldsymbol{s}}+3) \times (N_{\boldsymbol{s}}+3)$ *diagonal* matrix whose diagonal entries $\mathfrak{R}_{ll}^{(n)}$ are given by

$$\mathfrak{R}_{ll}^{(n)} = \begin{cases} \alpha_s^{(n)} & ; \quad 1 \leq l \leq N_s \\ \alpha_p^{(n)} & ; \quad N_s+1 \leq l \leq N_s+2 \\ \alpha_{\rho_s}^{(n)} & ; \quad l = N_s+3 \end{cases} \tag{29}$$

where the regularization parameters $\alpha_s^{(n)}, \alpha_p^{(n)}$ and $\alpha_{\rho_s}^{(n)}$ are positive numbers. At each iteration n, the "optimal" value of the triplet $(\alpha_s^{(n)}, \alpha_p^{(n)}, \alpha_{\rho_s}^{(n)})$ is obtained by sweeping each of the three regularization parameters over a large interval of positive numbers and evaluating the corresponding residuals, i.e., the relative errors, in the euclidean norm in $\mathbb{R}^{N_{\hat{x}}}$, between the measured intensity vector $\widetilde{\boldsymbol{U}}$ and the computed one $U\left(\boldsymbol{q}^{(n)}\right)$, and then selecting the value of the triplet that leads to the minimum residual (up to the noise level in the data). Note that we also monitor, at the same

time, the relative errors between two successive solutions $\boldsymbol{q}^{(n)}$ and $\boldsymbol{q}^{(n+1)}$ to determine whether or not the algorithm is stagnating, i.e., the algorithm is "trapped" at local minimum. Note that stagnation occurs when the successive relative error on the computed parameters is lower than a prescribed tolerance. In all the numerical experiments reported in Section 5, we have set this tolerance to be 0.1. Furthermore, we must point out that the proposed brute force approach for selecting, at each iteration, the "optimal" value of the regularization triplet is actually not a systematic three dimensional sweeping procedure that leads to a prohibitive computational cost. The proposed strategy consists in tracking, the "optimal" value along a one-dimensional curve. Indeed, after an appropriate initialization, we proceed in three steps. In each step, we vary the values of one regularization parameter while the values of the two others remain "frozen". More specifically, we proceed as follows:

- **Initialization: selecting an initial guess.** All three regularization parameters are chosen to be two order of magnitude greater than the largest diagonal entries of the normal system in (15), i.e., we set:

$$\alpha_s^{(0)} = \alpha_p^{(0)} = \alpha_{\rho_s}^{(0)} = 10^2 \max_{1 \leq l \leq N_{\boldsymbol{s}}+3} \left(J_U^* \left(\boldsymbol{q}^{(0)} \right) J_U \left(\boldsymbol{q}^{(0)} \right) \right)_{ll} \tag{30}$$

- **Step 1: Varying $\alpha_s^{(n)}$ only.** We start running the algorithm using the regularization matrix $\mathfrak{R}^{(0)}$. At each iteration, we evaluate the relative residual and the successive relative error. If stagnation occurs and/or the relative residual increases, then the value of $\alpha_s^{(n)}$ is reduced while the values of the two others remain unchanged, i.e., $\alpha_p^{(n)} = \alpha_p^{(0)}$ and $\alpha_{\rho_s}^{(n)} = \alpha_{\rho_s}^{(0)}$.

  A typical reduction factor of $\alpha_s^{(n)}$ employed in the experiments reported in Section 5 is 1/10. We continue iterating the algorithm and decreasing $\alpha_s^{(n)}$ until either convergence or stagnation is reached. At stagnation, we go to Step 2.

  We must point out that we have observed that only the sequence of the shape parameter vector $\boldsymbol{s}^{(n)}$ tends to converge, in this step, to the sought-after parameter $\boldsymbol{s}$.

- **Step 2: Varying $\alpha_p^{(n)}$ only.** This step is similar to Step 1. The only difference is that here the value of $\alpha_p^{(n)}$ varies whereas $\alpha_s^{(n)}$ remains frozen. Indeed, in this step, the value of $\alpha_{\rho_s}^{(n)}$ is still the initial value, i.e., $\alpha_{\rho_s}^{(n)} = \alpha_{\rho_s}^{(0)}$ and the value of $\alpha_s^{(n)}$ is set to be the last selected value in Step 1. We iterate the algorithm and decrease the value of $\alpha_p^{(n)}$ at each stagnation or oscillation of the relative residual. We continue until convergence or stagnation are reached. At stagnation, we go to Step 3.

  We have observed that at the end of this step, the sequence of material parameters $(\lambda^{(n)}, \mu^{(n)})$ tends to converge to the target parameter values (λ, μ).

- **Step 3: Varying $\alpha_{\rho_s}^{(n)}$ only.** We repeat exactly the same process described in Step 1 and Step 2. The only difference is that in this step, we decrease the value of $\alpha_{\rho_s}^{(n)}$ while setting the value of $\alpha_s^{(n)}$ (resp. $\alpha_p^{(n)}$) to be the last value selected in Step 1 (resp. Step 2).

  Note that at the end of Step 3, the density sequence $\rho_s^{(n)}$ tends to converge to the target value ρ_s.

  We must point out that in the event that the relative residual value does not reach the noise level, we repeat the full process starting with an initial guess for each parameter being the latest value selected at each corresponding step and using FFP measurements corresponding to a higher wavenumber k.

3.3.2 The Choice of $\mathfrak{R}^{(n)}$ in Stage II.

We recall that Stage II is dedicated to the determination of the location $\boldsymbol{x_c} = (x_c, y_c)$ using the regularized Newton equation given by (12)-(13). Therefore, the regularization matrix $\mathfrak{R}^{(n)}$ is a 2×2 diagonal matrix given by

$$\mathfrak{R}^{(n)} = \alpha_c^{(n)} \boldsymbol{I} \tag{31}$$

where $\boldsymbol{I}$ is the 2×2 identity matrix and $\alpha_c^{(n)}$ is a positive number representing the regularization parameter. Due to the small size of the linear system (13), the trial and error strategy for finding the optimal value of $\alpha_c^{(n)}$ is simpler and "cheaper" than in Stage I.

4 Algorithm Summary and Computational Complexity

The description of the proposed solution methodology is summarized in this section along with the required calculations that drive the computational cost for its implementation.

4.1 Algorithm Summary

The proposed multi-stage solution methodology for solving the inverse problem IOP(7) can be summarized as follows.

Stage 0: Initialization. The proposed regularization Newton algorithm requires the following initial data:

- A measured set of FFP, for one or several frequencies, at some observation points $\hat{\boldsymbol{x}}_{\boldsymbol{1}}, ..., \hat{\boldsymbol{x}}_{\boldsymbol{N_{\hat{x}}}}$, i.e., the FFP vector

  $$\widetilde{\boldsymbol{p_\infty}} = [\widetilde{p_\infty}(\hat{\boldsymbol{x}}_{\boldsymbol{1}}), ..., \widetilde{p_\infty}(\hat{\boldsymbol{x}}_{\boldsymbol{N_{\hat{x}}}})]^T \in \mathbb{C}^{N_{\hat{x}}}$$

  and its corresponding intensity

  $$\widetilde{\boldsymbol{U}} = \left[\mid \widetilde{\boldsymbol{p_\infty}}(\hat{\boldsymbol{x}}_{\boldsymbol{1}}) \mid^2, ..., \mid \widetilde{\boldsymbol{p_\infty}}(\hat{\boldsymbol{x}}_{\boldsymbol{N_{\hat{x}}}}) \mid^2 \right]^T$$

  The tilde indicates that these measurements are tainted with a *known* noise level.
- An initial parameter vector $\boldsymbol{q}^{(0)} = \left[\boldsymbol{s}^{(0)}, \lambda^{(0)}, \mu^{(0)}, \rho_s^{(0)} \right]^T \in \mathbb{R}^{N_s+3}$. The coordinates of the vector $\boldsymbol{q}^{(0)}$ are selected arbitrarily, i.e., $\boldsymbol{q}^{(0)}$ is a "blind" guess. Note that the initial location $\boldsymbol{x_c}^{(0)}$ of the scatterer is typically set to be the origin, that is, $\boldsymbol{x_c}^{(0)} = (0,0)^T$. We then construct the initial domain $\Omega_s^{(0)}$ and solve BVP(1) to deduce the FFP $p_\infty^{(0)}$ and its corresponding intensity $U^{(0)}$.

Stage 1: Retrieving simultaneously the shape and material parameters $\boldsymbol{q} = [\boldsymbol{s}, \lambda, \mu, \rho_s]^T$. For a given frequency, this stage requires accomplishing successively the following tasks:

- The construction, at each iteration n, of the Jacobian matrix $J_U(\boldsymbol{q}^{(n)})$ given by (16).
- The application of the regularized Newton algorithm given by (15) and (12) until convergence or stagnation is reached.

  Note that the regularization matrix $\mathfrak{R}^{(n)}$ is selected according to the procedure described in Section 3.3.1. Moreover, at each iteration n, the intensity field $\boldsymbol{U}(\boldsymbol{q}^{(n)})$ must be computed to monitor the algorithm convergence. If stagnation occurs, we

switch to a higher wavenumber k and repeat the procedure described in Stage 1 with an initial guess $\boldsymbol{q}^{(0)}$ being the computed value $\boldsymbol{q}^{(n)}$ at the stagnated iteration of the algorithm.

Stage 2: Recovering the location parameters, i.e., $\boldsymbol{q} = [x_c, y_c]^T$. The initial guess at this stage is $\boldsymbol{q}^{(0)} = [0,0]^T$ and the scatterer Ω_s corresponds to computed parameters $\left[\boldsymbol{s}^{(n)}, \lambda^{(n)}, \mu^{(n)}, \rho_s^{(n)}\right]^T$ at convergence in Stage 1. This stage requires accomplishing successively the following tasks:

- The construction, at each iteration n, of the Jacobian matrix $J_F(\boldsymbol{q}^{(n)})$ defined in Section 2.1.2.
- The application of the regularized Newton algorithm given by (14) and (12) until convergence or stagnation. Note that the regularization matrix $\mathfrak{R}^{(n)}$ is selected according to the procedure described in Section 3.3.2. Moreover, at each iteration n, the FFP $\boldsymbol{p_\infty}(\boldsymbol{q}^{(n)})$ must be computed to monitor the algorithm convergence.

4.2 Computational Complexity

The proposed multi-stage approach for solving IOP(7) mainly requires, for a given frequency, the following calculations.

Stage 0. Only one sparse linear system that results from the IPDG-discretization of BVP(6) (see section 3.2) needs to be solved. This is accomplished using an LU factorization, as indicated in Section 3.2.

Stage 1. Two linear systems need to be solved:

- One sparse linear system with $N_{\boldsymbol{s}} + 3$ different right-hand sides in order to build the Jacobian matrix needed for the regularized Newton equation (15).
- One small-size but full linear system ($(N_{\boldsymbol{s}} + 3) \times (N_{\boldsymbol{s}} + 3)$) to determine the update $\boldsymbol{\delta q}^{(n)}$. This is accomplished, for each selected regularization matrix (see Section 3.3.1), using LU-factorization.

Stage 2. Similarly to Stage 2, two linear systems need to be solved:

- One sparse linear system with two different right-hand sides in order to build the Jacobian matrix needed for the regularized Newton equation (14).
- A 2×2 linear system to determine the update $\boldsymbol{\delta q}^{(n)}$. This is accomplished for each selected regularized parameter α_c (see Section 3.3.2), using an analytical inversion.

5 Performance Assessment: Numerical Investigation

We investigate the convergence and the accuracy of the proposed multistage solution methodology, as well as its robustness to the noise level in the measurements. To this end, we consider synthetic FFP measurements corresponding to a single incident direction $\vec{d} = (1,0)$ but for one or multiple frequencies. The measured data are obtained by sampling the full aperture of the FFP at 360 points. They are contaminated with white noise of levels ranging from 0% to 15% to mimic possible errors in the measurements. In what follows, we report on the determination of the values of the parameters characterizing three non-convex elastic scatterers: (a) a disk, (b)

a non-convex octagon, and (c) a mockup-submarine. Note that the first two scatterers are made of *steel*, whereas the third one is made of *aluminum*.

We first analyze the performance of the algorithm when the synthetic measurements are noise-free. We then investigate its sensitivity to the noise level. Last, we present results to illustrate the importance of using multiple frequencies to improve both the convergence and the accuracy, particularly when retrieving the material parameters.

5.1 Performance analysis in the absence of the noise.

We present in this section numerical results to assess the performance efficiency of the proposed computational procedure when using noise-free synthetic FFP measurements. As stated earlier, these results have been obtained for three different scatterers: (a) a disk, (b) a non-convex octagon, and (c) a mockup-submarine.

5.1.1 Case of a disk-shaped scatterer.

As a proof of concept experiment, we consider here the simplest configuration: a disk-shaped domain made of *steel*. The synthetic FFP measurements are generated analytically using the Fourier series representation of the field [18, 27]. The FFP data have been measured at frequency $f = 71.61$kHz (i.e., $ka = 3$), which corresponds to a relatively low-medium frequency regime (see Fig. 3). The goal here is to determine the radius a, the material parameters (λ, μ, ρ), and the location center (x_c, y_c) of a disk made of *steel*. The values of these six sought-after parameters are reported in the first row of Table 1 and in Fig. 4.

Parameter	λ (GPa)	μ (GPa)	ρ_s ($kg\ m^{-3}$)	a (cm)	x_c (cm)	y_c (cm)
Target	115.40	76.90	7900	1.00	0.50	0.70
Initial guess	50.00	50.00	3000	0.50	0.00	0.00
Relative Error (%)	56.67	34.98	62.03	50	100	100

Table 1: Characteristic parameter values for the disk-shaped scatterer experiment. Target vs. Initial Guess.

In order to solve the considered six-parameter inverse problem (see (7)), we consider as an initial guess a disk whose characteristic parameter values are reported in the second row of Table 1 and in Fig. 4. The exterior boundary Σ (see (25)) is a circle of radius 7.5 cm, which appears to be, given the considered frequency regime, far enough to neglect the effect of possible wave reflections at Σ [9]. The resulting computational domain is discretized using an unstructured mesh of triangular-shaped elements with -at least- 5 points per elements (see Fig. 5). Similarly to [9], we employ the IPDG solver using polynomial shape functions of fifth order [24]. The results delivered by the proposed computational procedure are reported in Figs. 6-9 and Table 2. Recall that Stage I of the proposed algorithm uses the FFP intensity to deliver all the parameter values expect the location of the scatterer. The latter is retrieved in Stage II of the algorithm using the FFP. The following observations are noteworthy:

- The considered initial configuration (see Table 1) has been selected to ensure that the algorithm is *"blind"* to the sought-after parameter values. Indeed, the initial relative error on the radius (resp. the material parameters) is 50% (resp. 51%). The initial relative error on the location is about 100%. Consequently, the initial relative residual on the FFP

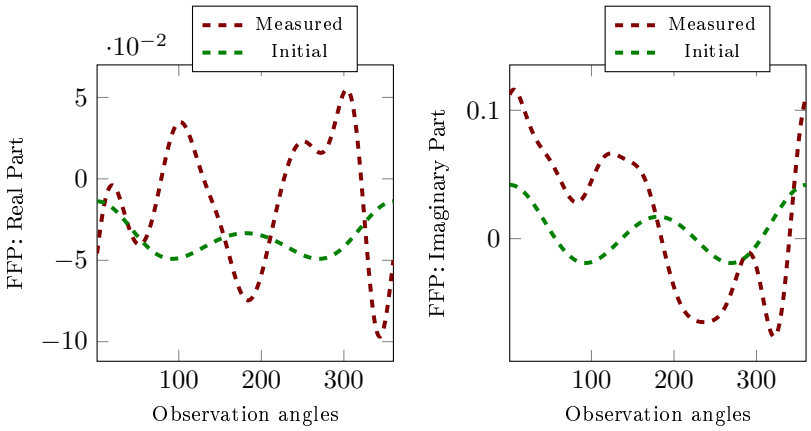

(a) Full FFP: Real and Imaginary Parts.

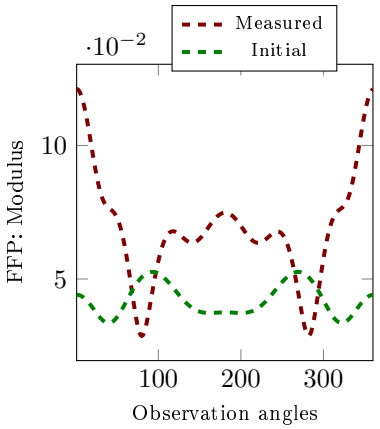

(b) Reduced FFP: Intensity.

Figure 3: FFP for the disk-shaped scatterer experiment. Target vs. Initial Guess. $f = 71.61$kHz and noise free measurements.

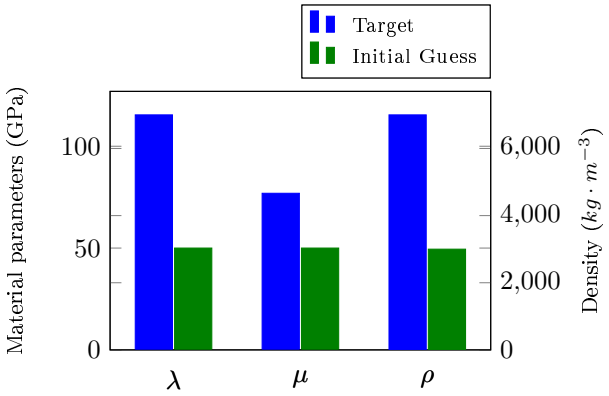

Figure 4: Material parameters for the disk-shaped scatterer experiment. Target vs. Initial Guess.

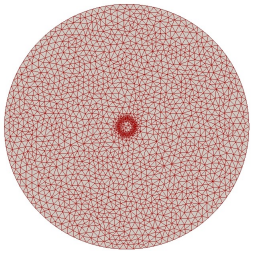

(a) Mesh with 3478 triangles.

Region	Γ^s	Γ^f	Ω^s	Ω^f
Number of triangles	56	56	112	3478

(b) Distribution of the triangles over the different computational domain regions.

Figure 5: Mesh resolution for the initial configuration of the computational domain for the disk shaped scatterer experiment.

intensity (resp. FFP) is over 80% (resp. 110%), as depicted in Fig. 3. Clearly, the proposed algorithm is applied outside the pre-asymptotic convergence region.

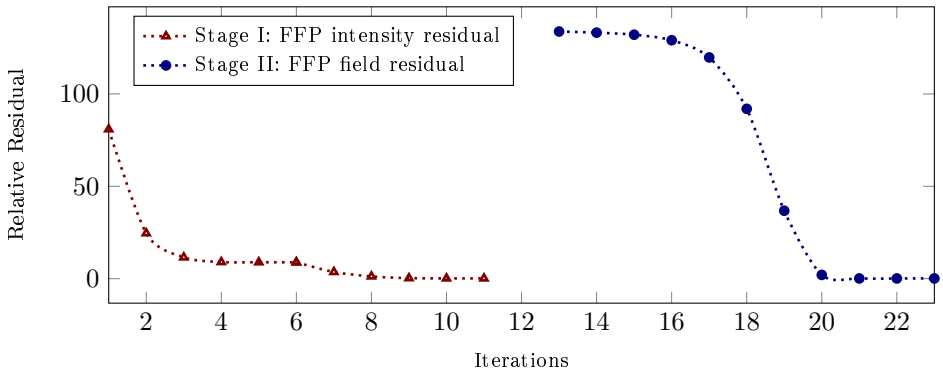

Figure 6: Convergence history in the case of a disk-shaped scatterer experiment. $f = 71.61$kHz and noise free measurements.

- Fig. 6 depicts the convergence performance of the proposed algorithm. It indicates that the convergence occurs after relatively a few iterations. More specifically, the convergence in Stage I, which corresponds to the determination of the shape and material parameters from the FFP intensity measurements, is attained in 11 iterations. The relative residual on the FFP intensity drops from 80% to below 0.2%, as depicted in Fig. 3(b) and Fig. 7(c). Note that the relative residual on the FFP is however over 130% (see Fig. 7(a)). Furthermore, the convergence in Stage II, which corresponds to the determination of the location from FFP measurements, is also achieved after 11 iterations. Indeed, the relative error on the FFP drops from 130% to below 0.1% (see Figs. 7(a),(b)).

- At convergence in Stage I the algorithm delivers the shape (resp. material) parameters with a relative error of about 0.07% (resp. 2%) (see Table 2 and Fig. 8(b)). Moreover, at convergence in Stage II, the algorithm determines the location of the scatterer with an accuracy level of about 0.01% (see Table 2 and Fig. 9(d)). Hence, the proposed algorithm retrieves the characteristic parameter values with a very high accuracy level.

Parameter	λ (GPa)	μ (GPa)	ρ_s $(kg\ m^{-3})$	a (cm)	x_c (cm)	y_c (cm)
Target	115.40	76.90	7900	1.00	0.50	0.70
Computed	113.52	76.96	7757.616	0.99	0.49	0.70
Relative Error	4.81	0.21	1.80	$7.59\ 10^{-2}$	$5.71\ 10^{-2}$	$2.97\ 10^{-5}$

Table 2: Characteristic parameter values for the disk-shaped scatterer experiment. Target vs. Computed Values at convergence in Stage II. $f = 71.61$kHz and noise free measurements.

- The algorithm encountered stagnation phases during the iterative process in both stages, as reported in Figs. 8-9. Lowering the regularization parameter values, via the trial and error approach, enables to overcome this phenomenon. Indeed, this change allowed the computational procedure to keep iterating up to the tolerated residual level, i.e., the noise level.

5.1.2 Case of an octogonal-shaped domain.

In this experiment, we determine the characteristic parameter values of a non-convex octagon elastic scatterer Ω^s immersed in water Ω^f (see Fig. 10(a)). The sought-after scatterer Ω^s is made of *steel* and its wet surface Γ is represented by the following piecewise linear parametrization:

$$\Gamma = \left\{ (x_c, y_c) + \sum_{j=1}^{8} (1-t)X_j + tX_{j+1} \quad ; \quad t \in [0,1] \right\} \tag{32}$$

where the vertices X_j are given by:

$$X_j = s_j \begin{pmatrix} \cos\theta_j \\ \sin\theta_j \end{pmatrix} \quad ; \qquad j = 1, ..., 8. \tag{33}$$

Note that the vertices are uniformly distributed in the polar coordinate angle. The values of the shape parameters s_j together with the center of the scatterer (x_c, y_c), as well as the material parameters (λ, μ, ρ) are reported in Table 3.
Unlike the previous experiment pertaining to the disk-shaped scatterer, the synthetic FFP measurements cannot be generated analytically. Therefore, they were computed (see Fig. 11) using the IPDG solver introduced in [9]. However, in order to avoid the inverse crime [27], we employed a mesh with a finer resolution than the one used during the inversion process (see Fig. 13 and Table 4).
In order to solve the considered thirteen-parameter inverse problem (see Eqs. (12), (14) and (15)), we considered as an initial guess a regular convex octagon elastic scatterer $\Omega^{(0)}$ (see Fig. 10(b)) whose characteristic parameter values are reported in Table 3 and Fig. 12. The corresponding initial FFP is depicted in Fig. 11. The results of this inversion experiment are reported in Figs. 14-18 and in Table 5. The following observations are worth-while:

- The initial guess for the parameters values has been selected outside the pre-asymptotic convergence region, ensuring that the algorithm is *"blind"* to the sought-after thirteen values of the parameters, as reported in Table 3. Indeed, the initial relative errors in the shape parameters, Lamé coefficients, density, and location of the scatterer, are 51.79%, 50.99%, 62.03%, 50%, respectively. These values lead to a computed initial FFP with a relative residual that exceeds 80% in the intensity (see Fig. 11(b)) and 115% in the FFP (see Fig. 11(a)).

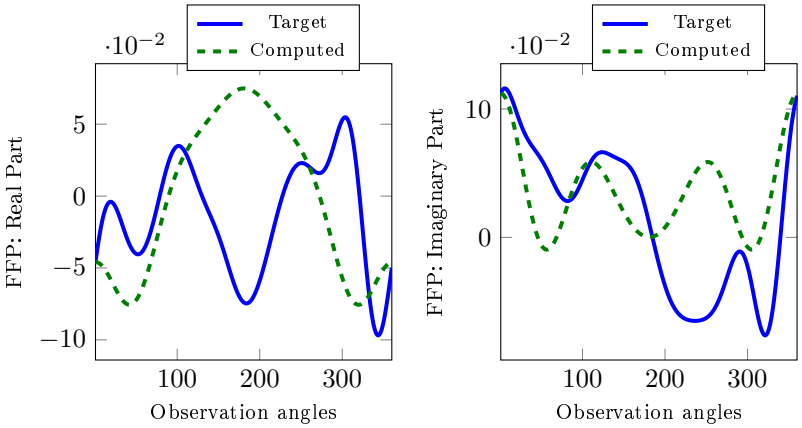

(a) Full FFP at convergence in Stage I.

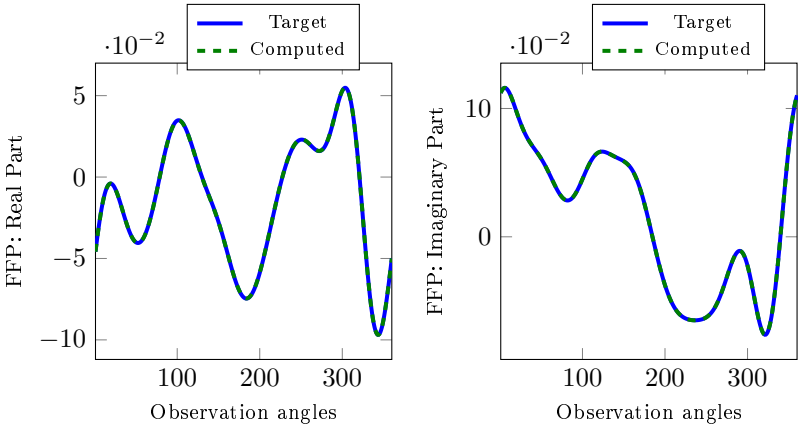

(b) Full FFP at convergence in Stage II.

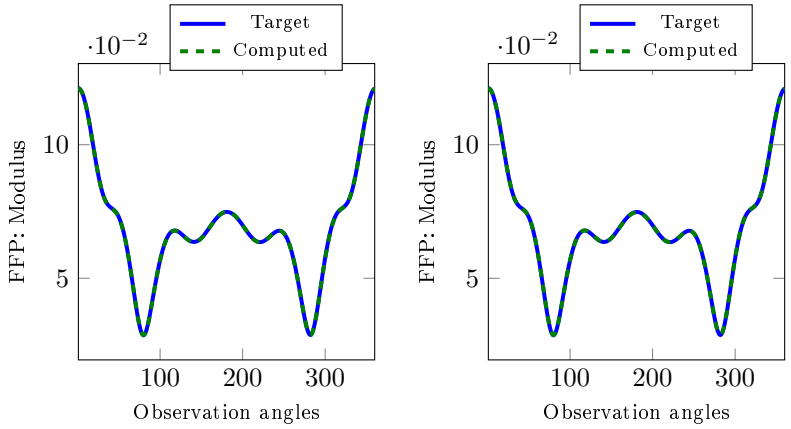

(c) FFP Intensity at convergence in Stage I.

(d) FFP Intensity at convergence in Stage II.

Figure 7: FFP for the disk-shaped scatterer experiment. Target vs. Computed Values at convergence. $f = 71.61$kHz and noise free measurements.

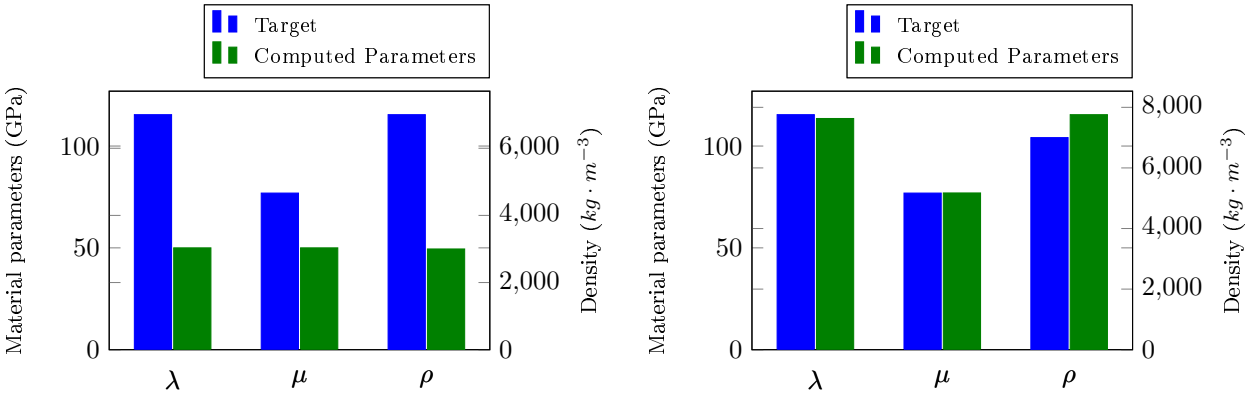

(a) Stage I: Iteration 5.

(b) Stage I: Iteration 11.

Figure 8: Material parameters for the disk-shaped scatterer experiment. Target vs. Computed Values at the occurred stagnation phases. $f = 71.61$kHz and noise free measurements.

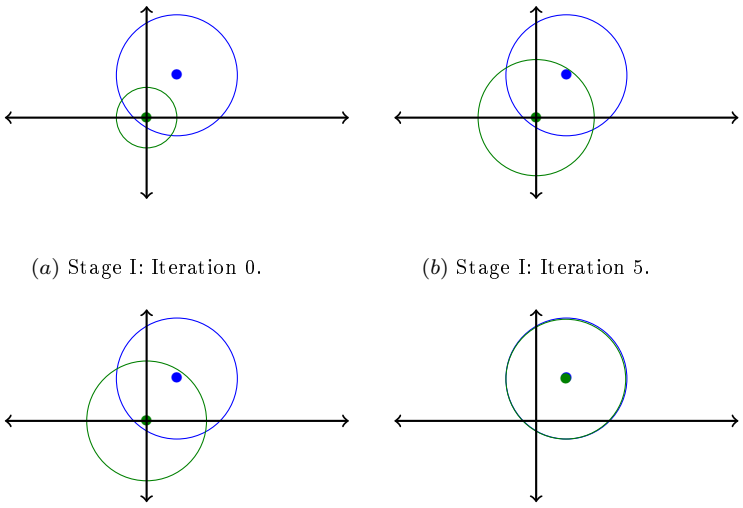

(*a*) Stage I: Iteration 0.

(*b*) Stage I: Iteration 5.

(*c*) Stage I: Iteration 11.

(*d*) Stage II: Iteration 11.

Figure 9: Shape and location of the disk-shaped scatterer experiment. Target vs. Computed Values at the occurred stagnation phases. $f = 71.61$kHz and noise free measurements.

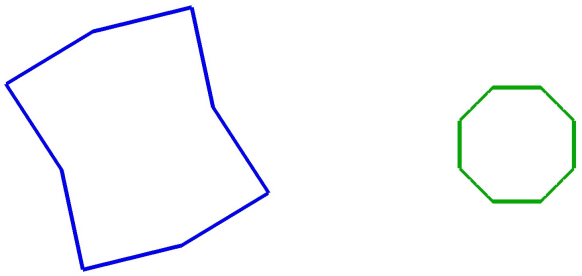

(a) Target (b) Initial guess

Figure 10: octogonal scatterers. Target vs. Initial Guess.

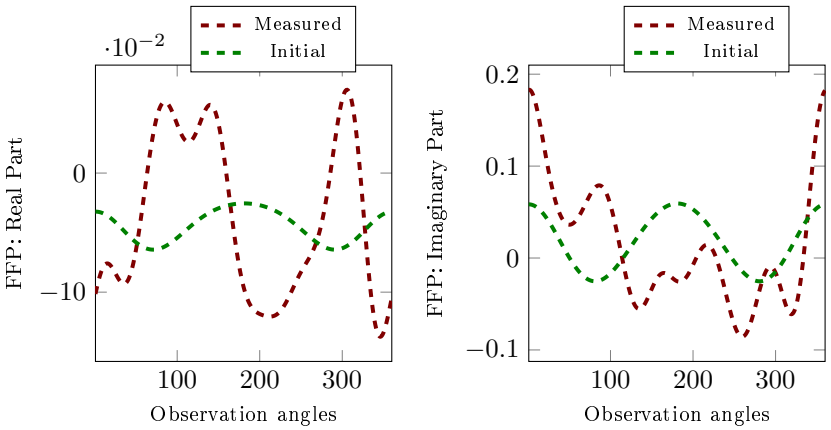

(a) Full FFP: Real and Imaginary Parts.

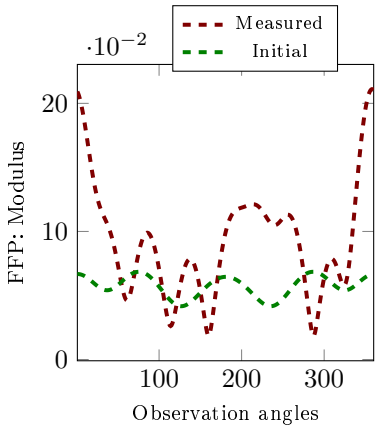

(b) Reduced FFP: Intensity.

Figure 11: FFP for the octogonal-shaped scatterer experiment. Target vs. Initial Guess. $f = 55.7$kHz and noise free measurements.

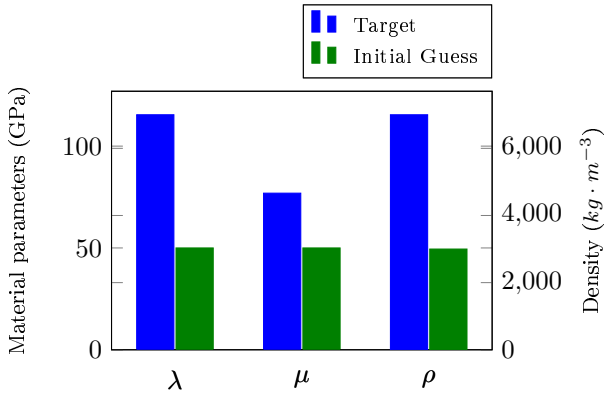

(a) Material parameter values.

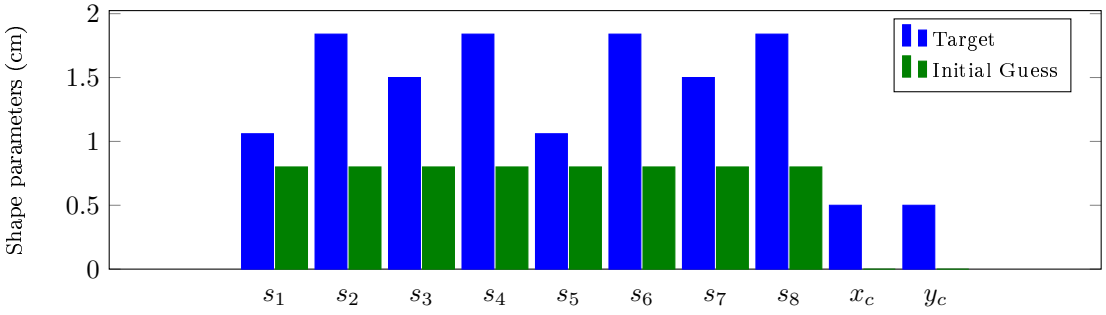

(b) Shape parameter values.

Figure 12: Characteristic parameter values for octogonal-shaped scatterer experiment. Target vs. Initial Guess.

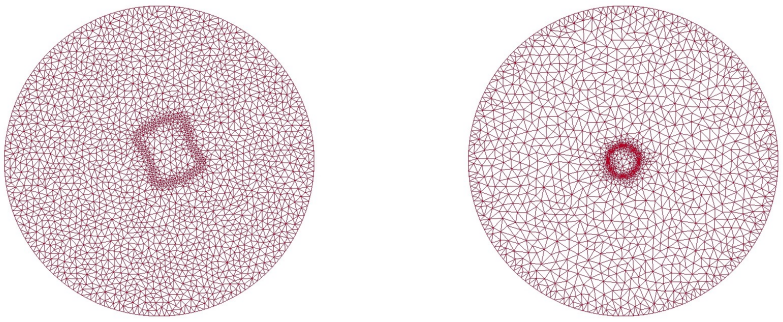

(a) Mesh 1: 4358 triangles.

(b) Mesh 2: 3088 triangles.

Figure 13: Mesh resolution for the synthetic measurements (left) and for the inversion procedure at the initial computational domain configuration (right).

Parameter	λ (GPa)	μ (GPa)	$\rho_s(kg\ m^{-3})$
Target	115.40	76.90	7900
Initial guess	50.00	50.00	3000
Relative Error (%)	56.67	34.98	62.03

(a) Material parameter values.

Parameter	s_1	s_2	s_3	s_4	s_5	s_6	s_7	s_8	x_c	y_c
Target (cm)	1.06	1.84	1.50	1.84	1.06	1.84	1.50	1.84	0.50	0.50
Initial guess (cm)	0.80	0.80	0.80	0.80	0.80	0.80	0.80	0.80	0.00	0.00
Relative Error (%)	24.58	56.52	46.67	56.52	24.57	56.52	46.67	56.52	100	100

(b) Shape and location parameter values.

Table 3: Characteristic parameter values for the octogonal-shaped scatterer experiment. Target vs. Initial Guess.

Region	Γ^s	Γ^f	Ω^s	Ω^f
Number of triangles for Mesh 1	96	92	308	3862
Number of triangles for Mesh 2	96	96	340	2556

Table 4: Distribution of the triangles over the different computational domain regions: Mesh 1 vs. Mesh 2.

- Fig. 14 illustrates the convergence performance of the algorithm. More specifically, the determination of the shape and material parameters (in Stage I) is completed in about 18 iterations. The relative residual on the FFP intensity drops from above 80% to below 1% (see Figure 15(c)). In Stage II, i.e., the determination of the location, the relative residual on the FFP drops from above 115% to below 1% in 13 iterations (see Figure 15(b)).

- At convergence in Stage I the algorithm delivers the shape parameters, the Lamé coefficients, and the density with relative errors of 0.08%, 2% and 0.5%, respectively (see Table 5 and Figs. 16(e)-17(e)). At convergence, i.e., at the end of Stage II, the location of the scatterer is retrieved with a relative error of about 2% (see Fig. 17(g) and Table 5). Clearly, the proposed algorithm recovers the parameter values with an impressive accuracy level.

- Similarly to the disk experiment, stagnation phases occurred during the iterative process (see Figs. 16(a)-(e) and Figs. 17(a)-(e)). Lowering the regularized parameter values each time helped the algorithm to proceed with the convergence toward the residual tolerance level.

5.1.3 Case of a mockup submarine.

The goal here is to retrieve the characteristic parameter values of a mockup submarine made of *aluminum* (see 19(a)). The wet surface Γ of the considered elastic scatterer is parametrized

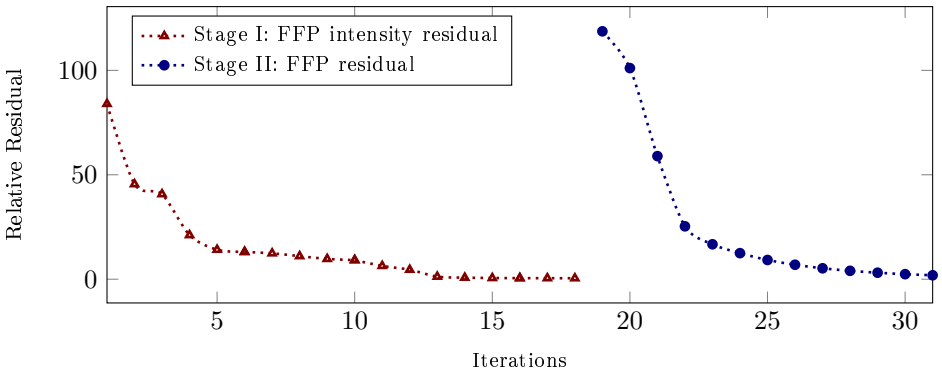

Figure 14: Convergence history in the case of the octogonal-shape scatterer experiment. $f = 55.7$kHz and noise free measurements.

Parameter	λ(GPa)	μ(GPa)	$\rho_s(kg\ m^{-3})$
Target	115.40	76.90	7900
Computed	111.78	76.23	7793.42
Relative Error (%)	3.13	0.86	1.34

(a) Material parameter values.

Parameter	s_1	s_2	s_3	s_4	s_5	s_6	s_7	s_8	x_c	y_c
Target (cm)	1.06	1.84	1.50	1.84	1.06	1.84	1.50	1.84	0.50	0.50
Computed (cm)	1.06	1.84	1.50	1.83	1.06	1.83	1.50	1.84	0.49	0.48
Relative Error (%)	0.29	0.04	0.06	0.01	0.01	0.01	0.06	0.07	1.01	2.56

(b) Shape and location parameter values.

Table 5: Characteristic parameter values of the octogonal-shaped scatterer experiment. Target vs. Computed Values at convergence. $f = 55.7$kHz and noise free measurements.

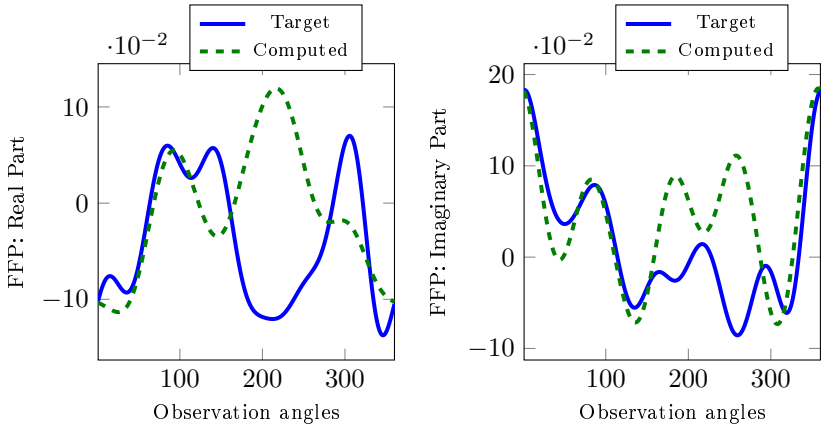

(a) Full FFP at convergence in Stage I.

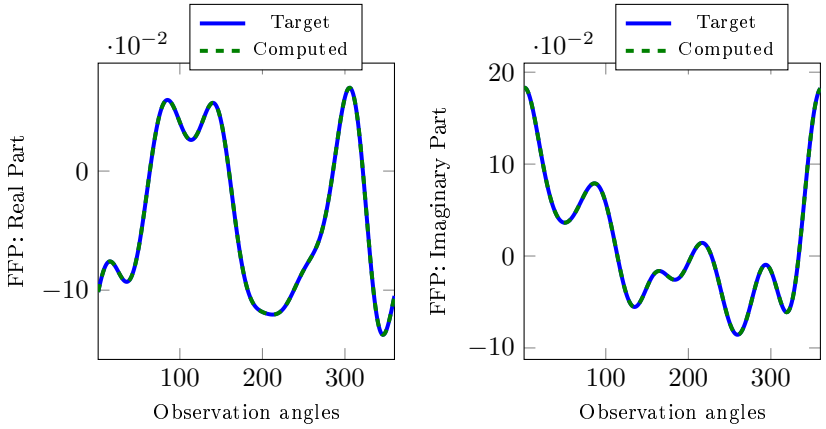

(b) Full FFP at convergence in Stage II.

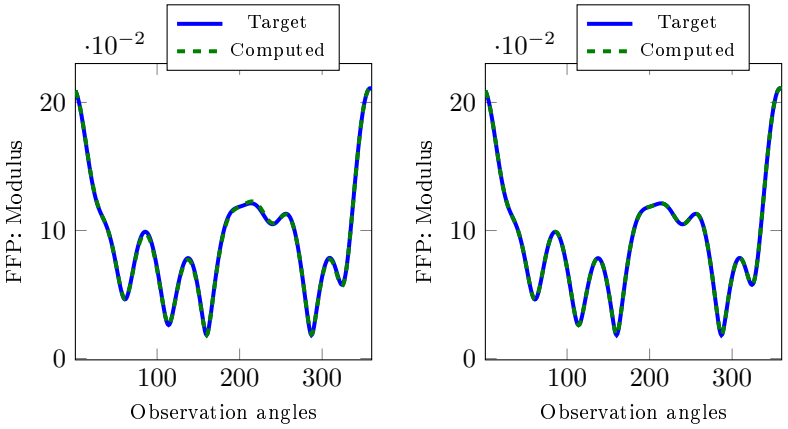

(c) FFP Intensity at convergence in Stage I.

(d) FFP Intensity at convergence in Stage II.

Figure 15: FFP for the octogonal-shaped satterer experiment. Target vs. Computed Values at convergence. $f = 55.7$kHz and noise free measurements.

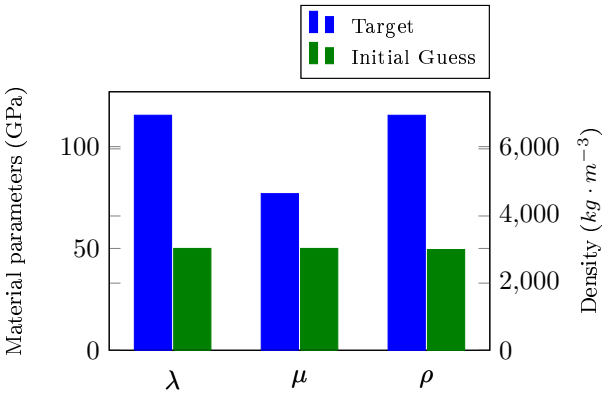

(a) Stage I: Iteration 0.

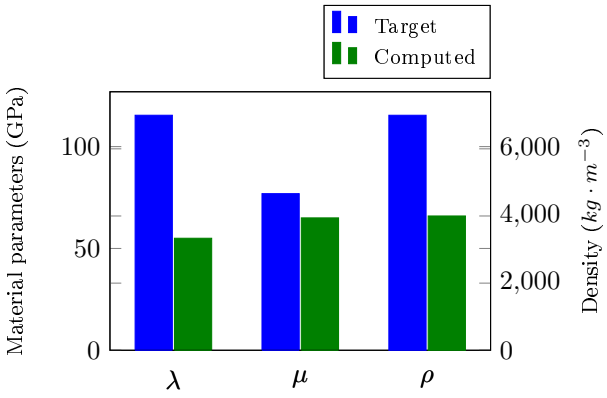

(b) Stage I: Iteration 6.

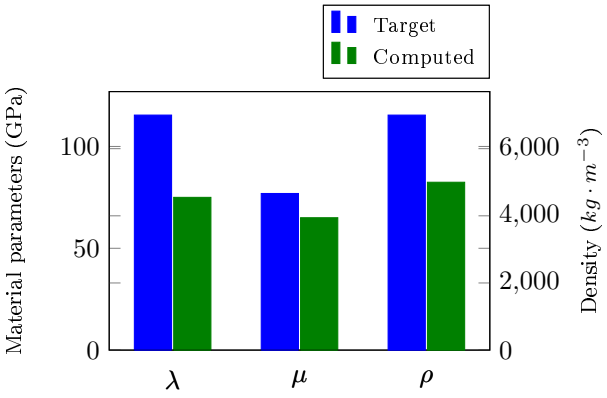

(c) Stage I: Iteration 10.

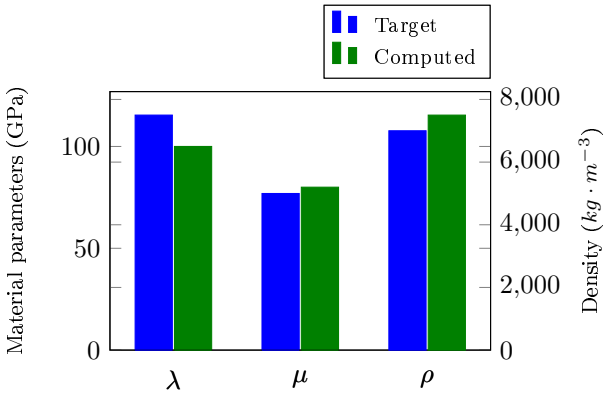

(d) Stage I: Iteration 16.

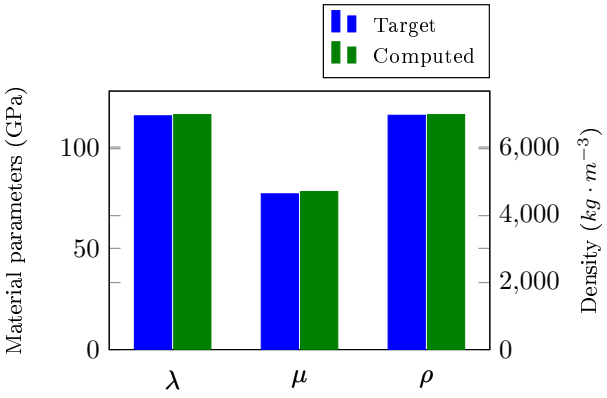

(e) Stage I: Iteration 18.

Figure 16: Material parameters for the octogonal-shaped scatterer experiment. Target vs. Computed Values at the occurred stagnation phases in Stage I. $f = 55.7$kHz and noise free measurements.

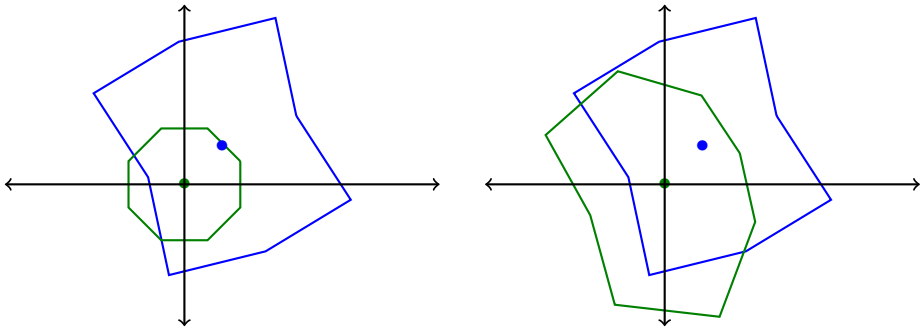

(*a*) Stage I: Iteration 0.

(*b*) Stage I: Iteration 6.

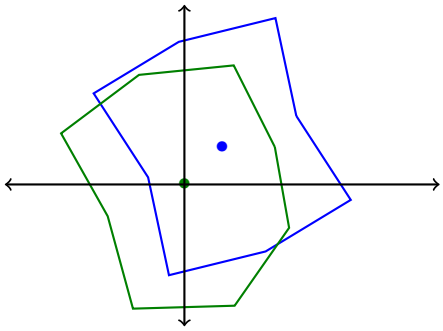

(*c*) Stage I: Iteration 10.

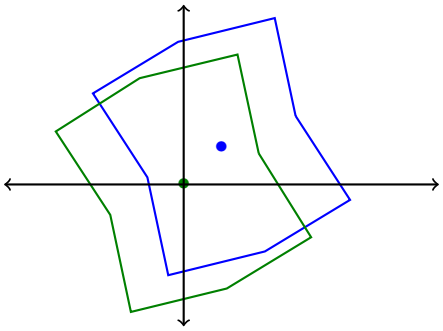

(*d*) Stage I: Iteration 16.

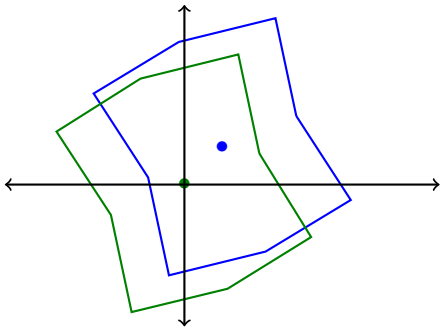

(*e*) Stage I: Iteration 18.

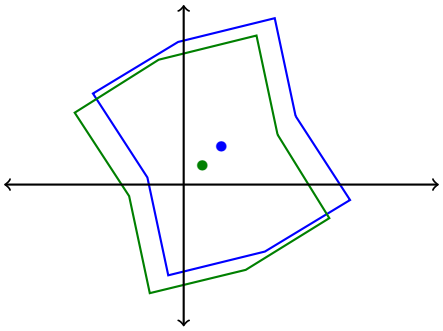

(*f*) Stage II: Iteration 5.

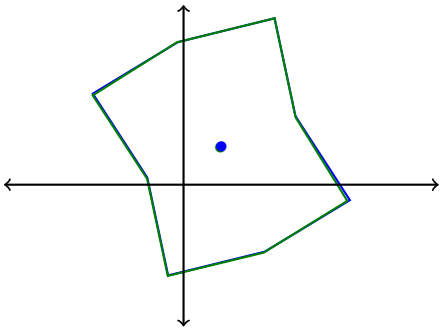

(*g*) Stage II: Iteration 13.

Figure 17: Shape and location of the octogonal-shaped scatterer experiment. Target vs. Computed Values at the occurred stagnations. $f = 55.7$kHz and noise free measurements.

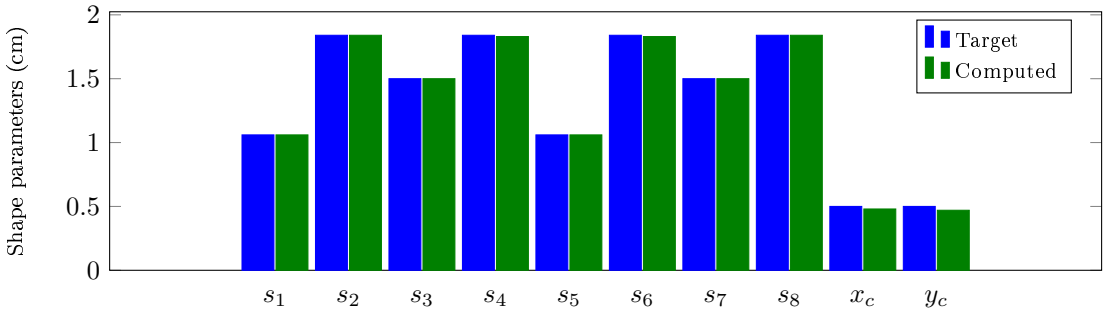

Figure 18: Characteristic shape parameter values of the octogonal-shaped scatterer experiment. Target vs. Computed Values at convergence. $f = 55.7$kHz and noise free measurements.

using the following Fourier expansions:

$$\Gamma = \left\{ (x_{ref}, y_{ref}) + s_0 + \sum_{k=1}^{M} s_{2k-1}\cos\theta + s_{2k}\sin\theta \quad ; \quad \theta \in [0, 2\pi) \right\} \tag{34}$$

The values of the shape parameters s_j together with the center of the scatterer (x_c, y_c), as well as the material parameters (λ, μ, ρ) are reported in Table 6 and Fig. 20.

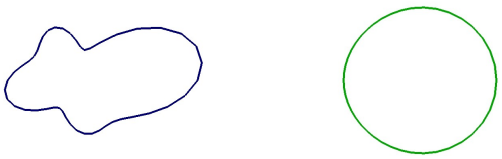

(a) Target scatterer (b) Initial scatterer

Figure 19: Shape configurations for the mockup submarine experiments: Target vs. Initial Guess.

Similarly to the previous experiment pertaining to the non-convex octogonal scatterer, we have generated the synthetic FFP measurements points at frequency $f = 55.7$kHz (see Fig. 21) using the IPDG solver introduced in [9]. Here again, in order to avoid the inverse crime [27], we employed a mesh finer than the one used during the inversion process, as indicated in Fig. 22 and Table 7.

To solve the resulting fourteen-parameter inverse problem (see Eqs. (12), (14) and (15)), we applied the proposed multistage algorithm starting from an initial configuration $\Omega^{(0)}$ set to be a disk-shaped domain (see Fig. 19(b)). The characteristic parameter values of $\Omega^{(0)}$ are reported in Table 6 and Fig. 20, and its corresponding FFP is depicted in Fig. 21. The results of this numerical experiment are reported in Table 8 and Figs. 23-26. The following observations are noteworthy:

- The proposed algorithm is initiated outside the pre-asymptotic convergence region. Indeed, the considered initial configuration, a disk-shaped domain, differs significantly from the

Parameter	λ (GPa)	μ (GPa)	ρ_s $(kg\ m^{-3})$
Target	51.09	26.31	2700
Initial guess	30.00	50.00	5000
Relative Error (%)	41.27	89.99	85.18

(a) Material parameter values.

Parameter	s_1	s_2	s_3	s_4	s_5	s_6	s_7	s_8	s_9	x_c	y_c
Target (cm)	1.50	0.50	0.05	0.60	0.01	0.20	0.10	0.20	0.30	0.2	1.5
Initial guess (cm)	1.75	0.60	0.00	0.10	0.00	0.00	0.00	0.00	0.00	0.00	0.00
Relative Error (%)	16.67	20	100	83.33	100	100	100	100	100	100	100

(b) Shape and location parameter values.

Table 6: Characteristic parameter values for the mockup submarine scatterer experiment. Target vs. Initial Guess.

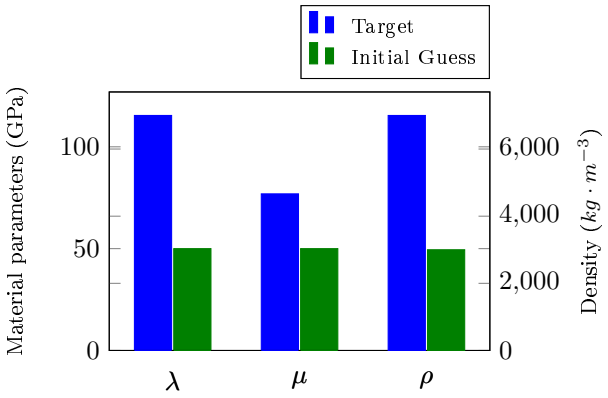

(a) Material parameter values.

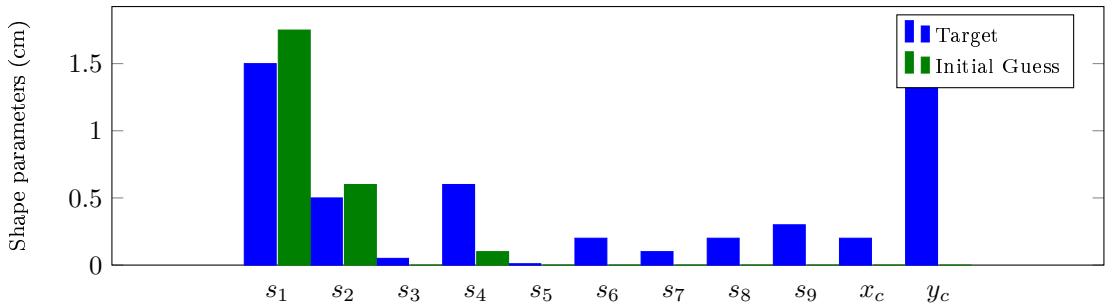

(b) Shape parameter values.

Figure 20: Characteristic parameter values for the mockup submarine scatterer experiment. Target vs. Initial Guess.

target configuration (see Table 6 and Figs. 20, 26(a)). The initial relative errors on the shape parameters, position parameter, Lamé coefficients, and the density are 40.74%, 100%, 55.19%, and 85.18%, respectively. The initial relative residual on the FFP is of about 63% on the intensity (see Fig. 21(b)) and of about 120% on the field (see Fig. 21(a)).

- The convergence of the algorithm in this case is clearly demonstrated in Fig. 23. More specifically, Stage I is completed in 24 iterations. The relative residual on the FFP intensity drops from 63% to 0.17% (see Fig. 24(c)). Furthermore, the algorithm converges in Stage II in 10 iterations. The relative residual on the FFP drops from 152% to 0.57% (see Figs. 24(a),(b)).

- Similarly to the previous two experiments (the disk- and octogonal- shaped scatterers), the algorithm recovers the fourteen sought-after parameters with an impressive accuracy level. Indeed, the relative errors on the computed shape parameters, Lamé coefficients, and the density are 0.43%, 1.02%, and 2.73%, respectively (see Table 8 and Fig. 25). The center (x_c, y_c) of submarine is recovered with a relative error of about 0.12% (see Table 8, Fig. 26).

- The stagnation phenomenon also occurs here at several steps during the iteration process (see Figs. 25-26). This phenomenon is treated each time it happened by lowering the value of the regularization parameter via the trial and error procedure.

- In all of the three experiments (disk, octagon, mockup-submarine), the proposed multistage strategy algorithm was able to successfully recover all the parameters from the knowledge of the FFP measurements corresponding to only one incident plane wave (i.e., one incident direction and one done frequency). This success is most likely due to the fact that the employed data are measured over the full aperture.

Region	Γ^s	Γ^f	Ω^s	Ω^f
Number of triangles for Mesh 1	70	70	140	4920
Number of triangles for Mesh 2	52	52	105	2726

Table 7: Distribution of the triangles over the different computational domain regions: Mesh 1 vs. Mesh 2.

5.2 Performance analysis in the presence of noise.

In what follows, we investigate the robustness and the accuracy of the proposed multistage solution methodology to the noise effect. To this end, we present illustrative numerical results corresponding to two configurations: a disk and an octagon.

5.2.1 Case of a disk-shaped domain.

We consider the same configuration adopted in the numerical experiment described in Section 5.1.1, i.e., a disk-shaped domain made of *steel* whose characteristic parameter values are reported in Table 1. The synthetic FFP measurements generated at frequency $f = 71.61$kHz (see Fig. 3) are however tainted with white noise to include possible errors in the measurements. Specifically, we add to the FFP measured vector white noise of levels ranging from medium (5%), to high

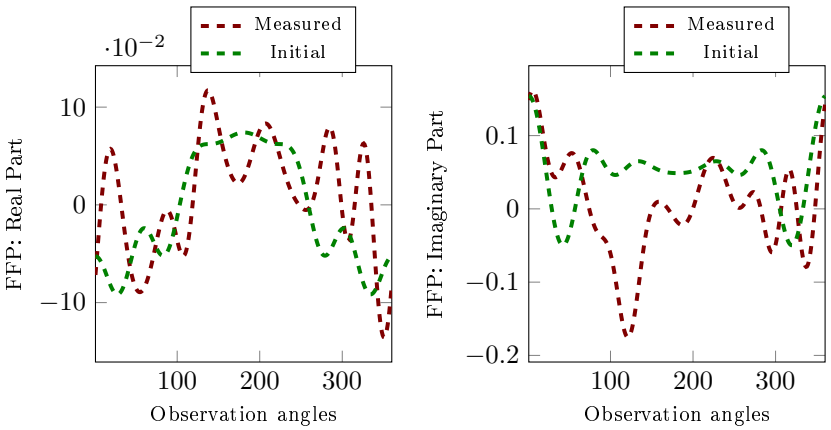

(a) Full FFP: Real and Imaginary Parts.

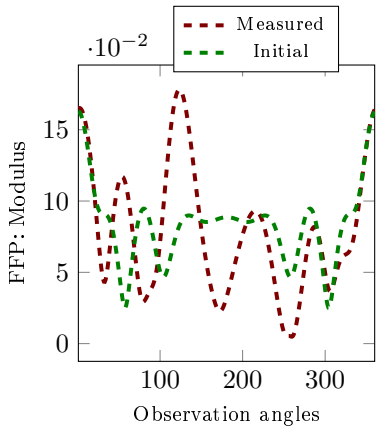

(b) Reduced FFP: Intensity.

Figure 21: FFP for the mockup submarine scatterer experiment. Target vs. Initial Guess. $f = 55.7$kHz and noise free measurements.

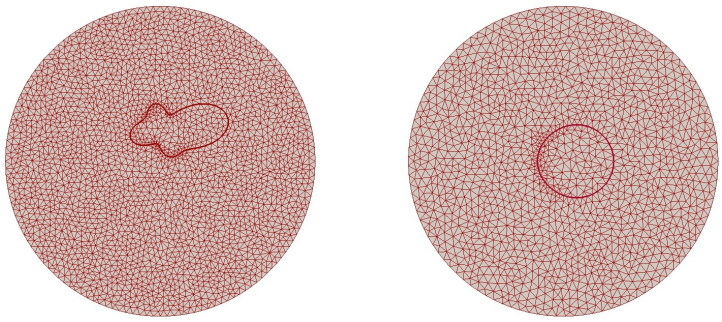

(a) Target: 5060 elements (b) Initial guess: 2831 elements

Figure 22: Mesh resolution for the synthetic measurements (left) and for the inversion procedure at the initial computational domain configuration (right).

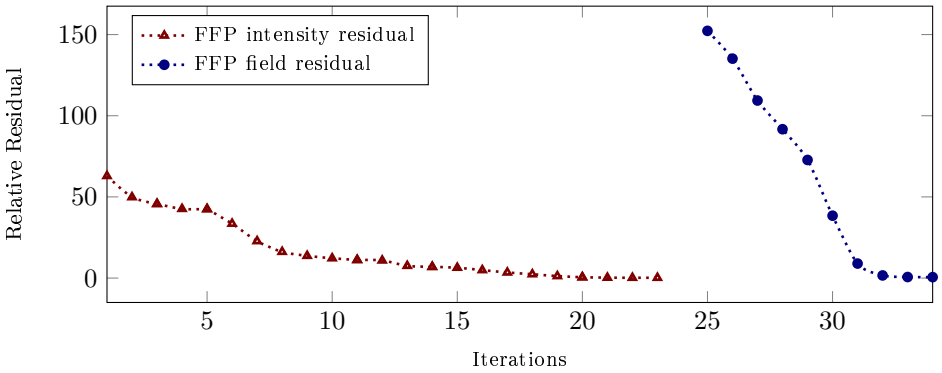

Figure 23: Convergence history for the mockup submarine scatterer experiment. $f = 55.7$kHz and noise free experiments.

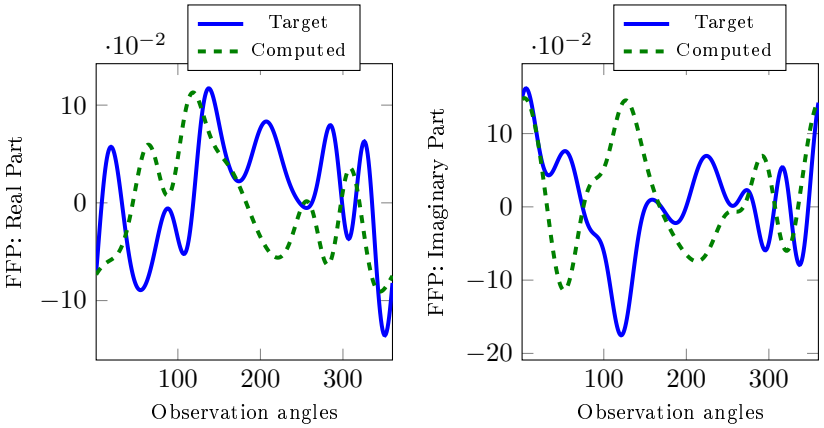

(a) Full FFP at convergence in Stage I.

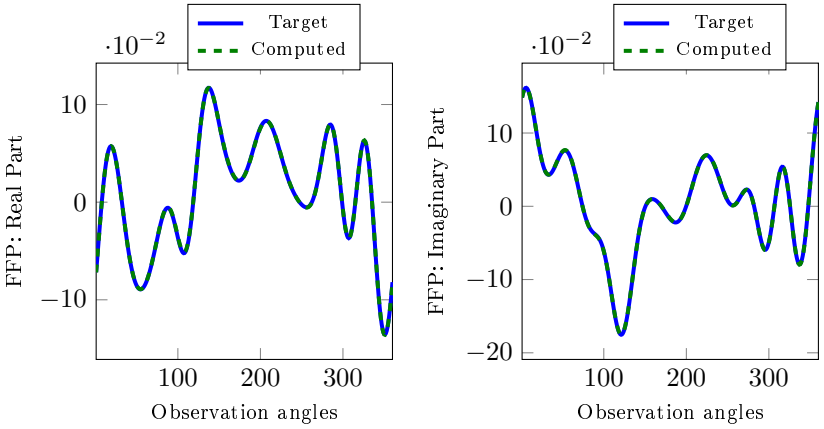

(b) Full FFP at convergence in Stage II.

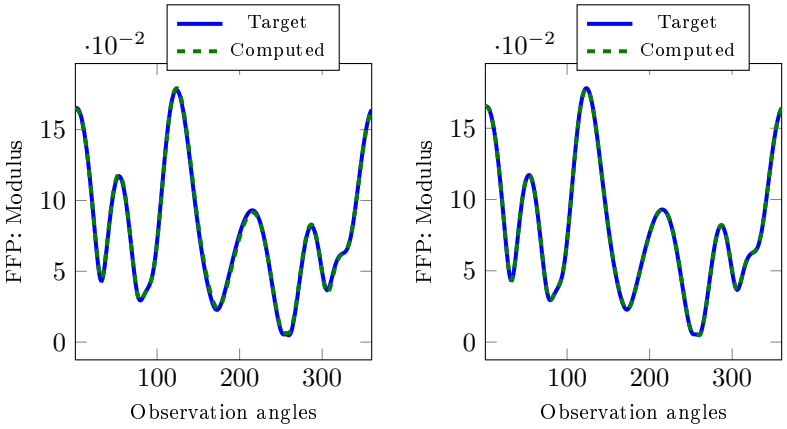

(c) FFP Intensity at convergence in Stage I.

(d) FFP Intensity at convergence in Stage II.

Figure 24: FFP for the mockup submarine scatterer experiment. Target vs. Computed Values at convergence. $f = 55.7$kHz and noise free measurements.

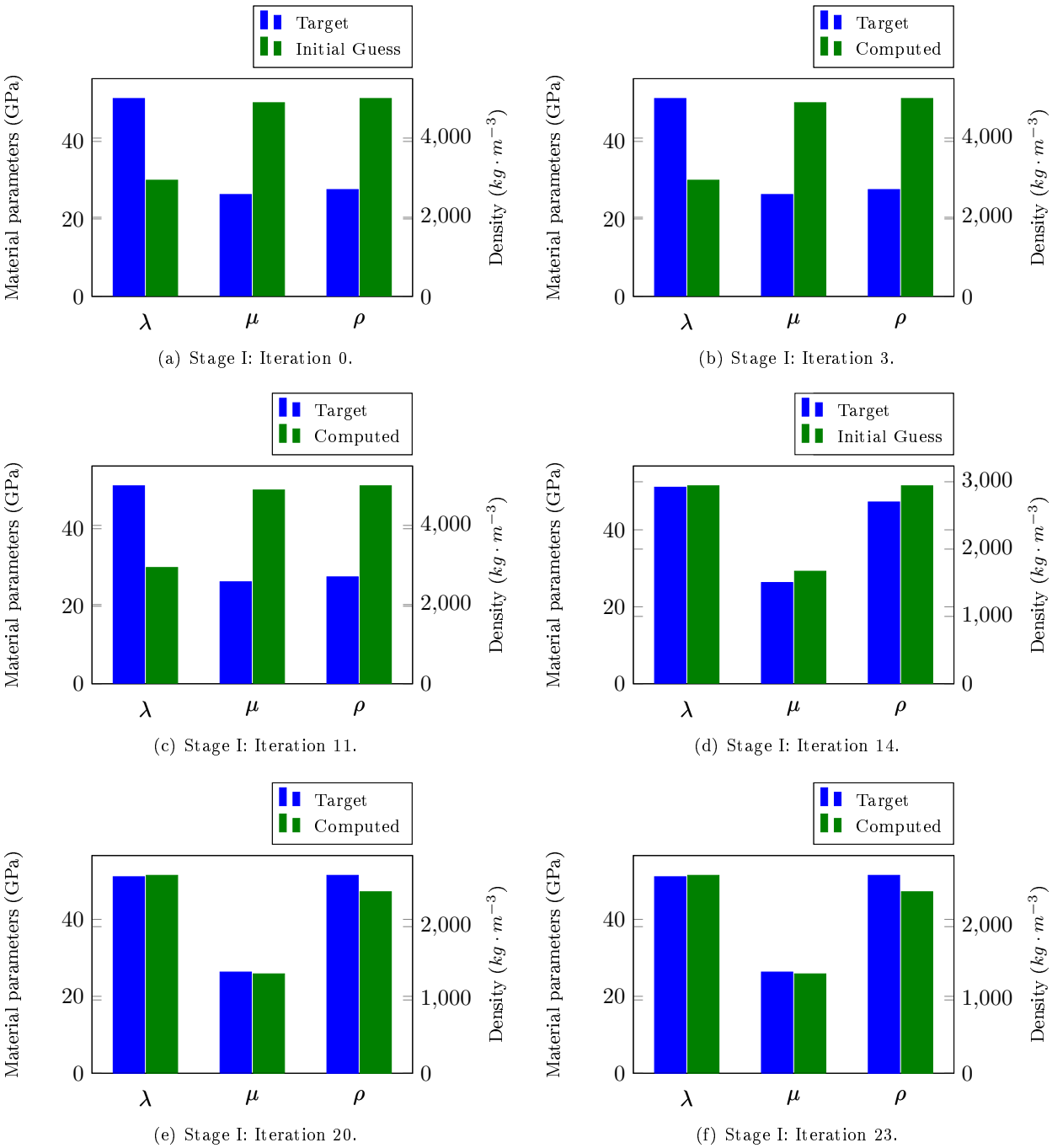

(a) Stage I: Iteration 0.

(b) Stage I: Iteration 3.

(c) Stage I: Iteration 11.

(d) Stage I: Iteration 14.

(e) Stage I: Iteration 20.

(f) Stage I: Iteration 23.

Figure 25: Material parameters for the mockup submarine scatterer experiment. Target vs. Computed Values at the occurred stagnation phases in Stage I. $f = 55.7$kHz and noise free measurements.

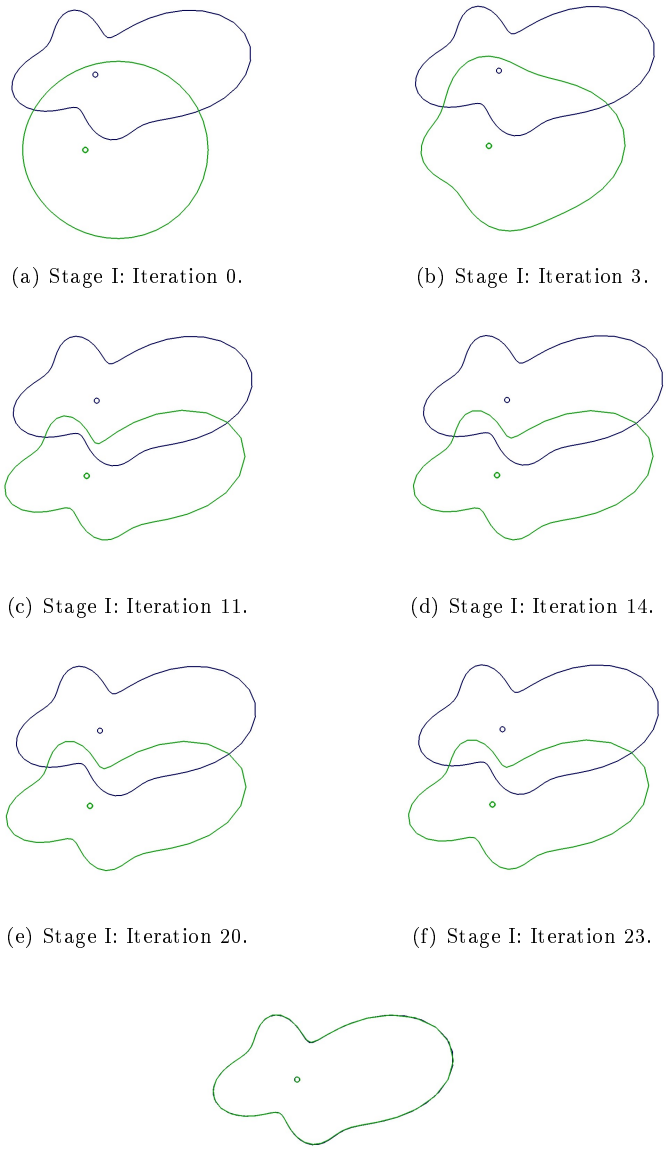

(a) Stage I: Iteration 0.

(b) Stage I: Iteration 3.

(c) Stage I: Iteration 11.

(d) Stage I: Iteration 14.

(e) Stage I: Iteration 20.

(f) Stage I: Iteration 23.

(g) Stage II: Iteration 10.

Figure 26: Shape and location for the mockup submarine scatterer experiment. Target vs. Computed Values at the occurred stagnations. $f = 55.7$kHz and noise free measurements.

Parameter	λ (GPa)	μ (GPa)	ρ_s $(kg\ m^{-3})$
Target	51.09	26.31	2700
Computed	48.23	26.34	2668
Relative Error (%)	5.57	0.08	1.15

(a) Material parameter values.

Parameter	s_1	s_2	s_3	s_4	s_5	s_6	s_7	s_8	s_9	x_c	y_c
Target (cm)	1.50	0.50	0.05	0.60	0.01	0.20	0.10	0.20	0.30	0.2	1.5
Computed (cm)	1.50	0.49	0.05	0.59	0.01	0.20	0.09	0.19	0.30	0.2	1.49
Relative Error (%)	0.08	0.31	11.86	0.05	35.80	0.76	1.37	0.44	0.06	0.31	0.11

(b) Shape and location parameter values.

Table 8: Characteristic parameter values for the mockup submarine scatterer experiment. Target vs. Computed Values at convergence. $f = 55.7$kHz and noise free measurements.

(10%), and to very high (15%), as depicted in Figs. 27-28.

For each considered noisy FFP measured vector, we applied the proposed multistage algorithm from the same initial configuration (see Table 1 and Figs. 3-4). The results of these three numerical experiments are reported in Figs. 29-33 and Table 9. These results indicate the following.

- For all the considered white noise levels in the FFP data, the algorithm is initiated outside the pre-asymptotic convergence region (see Table 1). The initial configuration differs significantly from the target one, leading to an initial relative residual over 80% for the intensity and over 110% for the full FFP.
- Fig. 29 and Table 9 reveal that, in the three experiments, the convergence is achievable to the prescribed noise levels. Fig. 29 indicates that, in all three cases, the convergence is attained after at most 12 iterations in each stage.
- Figs. 30-33 and Table 9 indicate that, for all considered noise levels, the proposed solution strategy is able to retrieve all the parameters with a quite remarkable accuracy level. For example, even when the data are contaminated with a high noise level (10%), the proposed method recovers the shape and the location parameters with a relative error less than 5%. In addition, the material parameters are obtained with a relative error of about 10% for the Lamé coefficients and about 12% for the density (see Table 9). Furthermore, Figs. 32-33 provide a comparison between the FFP corresponding to the target configuration and the one delivered by the proposed method at convergence. These figures also illustrate clearly the high accuracy level of the proposed inversion procedure.

5.2.2 Case of an octogonal-shaped scatterer.

We analyze here the noise effect on the determination of the characteristic parameter values corresponding to the non convex elastic scatterer described in Fig. 10(a) and Table 3. To this end, we consider the same numerical experiment set up presented in section 5.1.2. The only

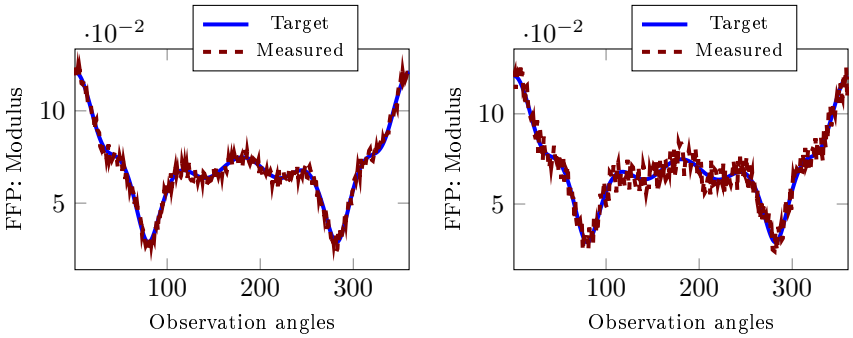

(a) Noise level 5%.

(b) Noise level 10%.

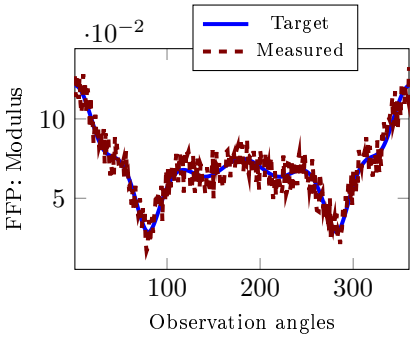

(c) Noise level 15%.

Figure 27: FFP intensity for disk-shaped scatterer experiments. Target vs. Measured. $f = 71.61$kHz and noise levels in the measurements: $5\%, 10\%, 15\%$.

Noise level	Relative Residual (%)		Relative Error (%)			
	Intensity	Field	Shape	Lamé	Density	Location
0%	0.21	0.11	$7.59\ 10^{-2}$	1.36	1.80	0.01
5%	6.06	5.07	0.36	3.43	1.38	0.48
10%	11.75	9.95	0.57	5.06	3.41	0.42
15%	17.36	14.88	0.60	6.97	9.85	0.64

Table 9: Final relative residual and relative errors, sensitivity to the noise level in the measurements $f = 71.61$kHz for the disk-shaped scatterer experiments.

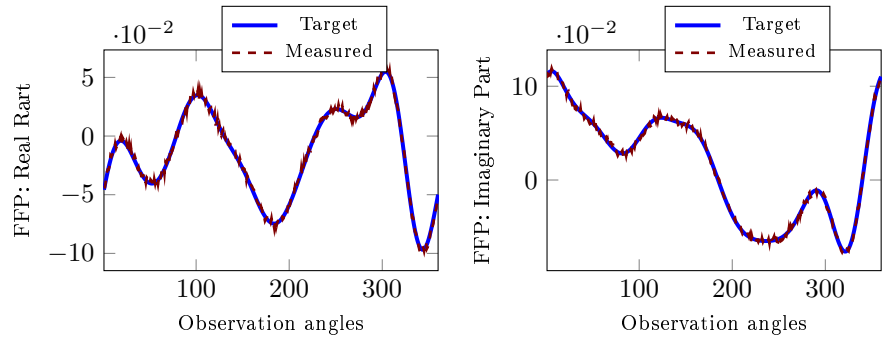

(a) Noise level 5%.

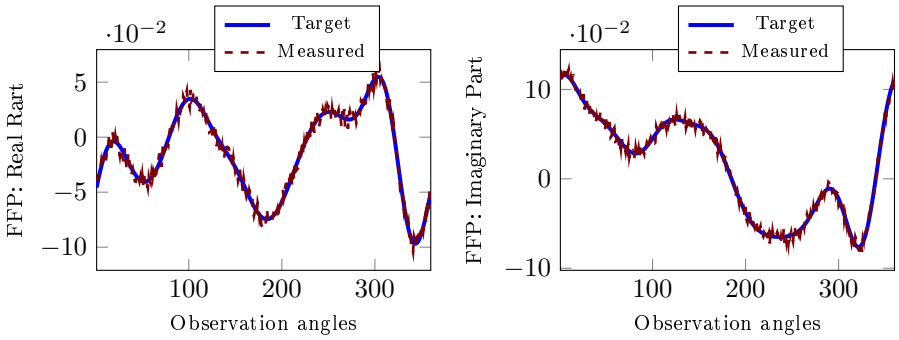

(b) Noise level 10%.

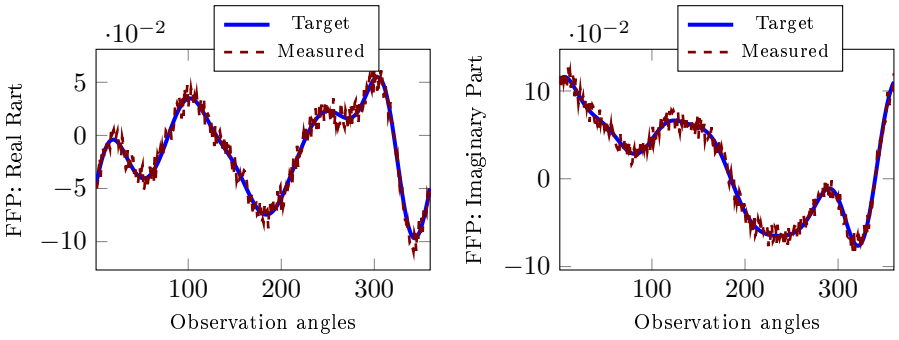

(c) Noise level 15%.

Figure 28: Full FFP for disk-shaped scatterer experiments. Target vs. Measured. $f = 71.61$kHz and noise levels in the measurements: $5\%, 10\%, 15\%$.

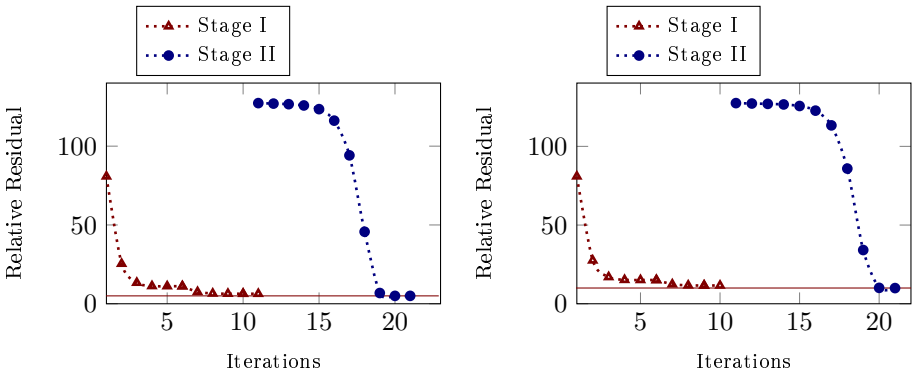

(a) Noise level 5%.

(b) Noise level 10%.

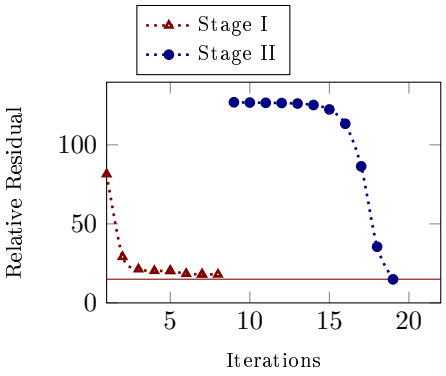

(c) Noise level 15%.

Figure 29: Convergence history for the disk-shaped scatterer experiments. Sensitivity to the noise level in the measurements $f = 71.61$kHz.

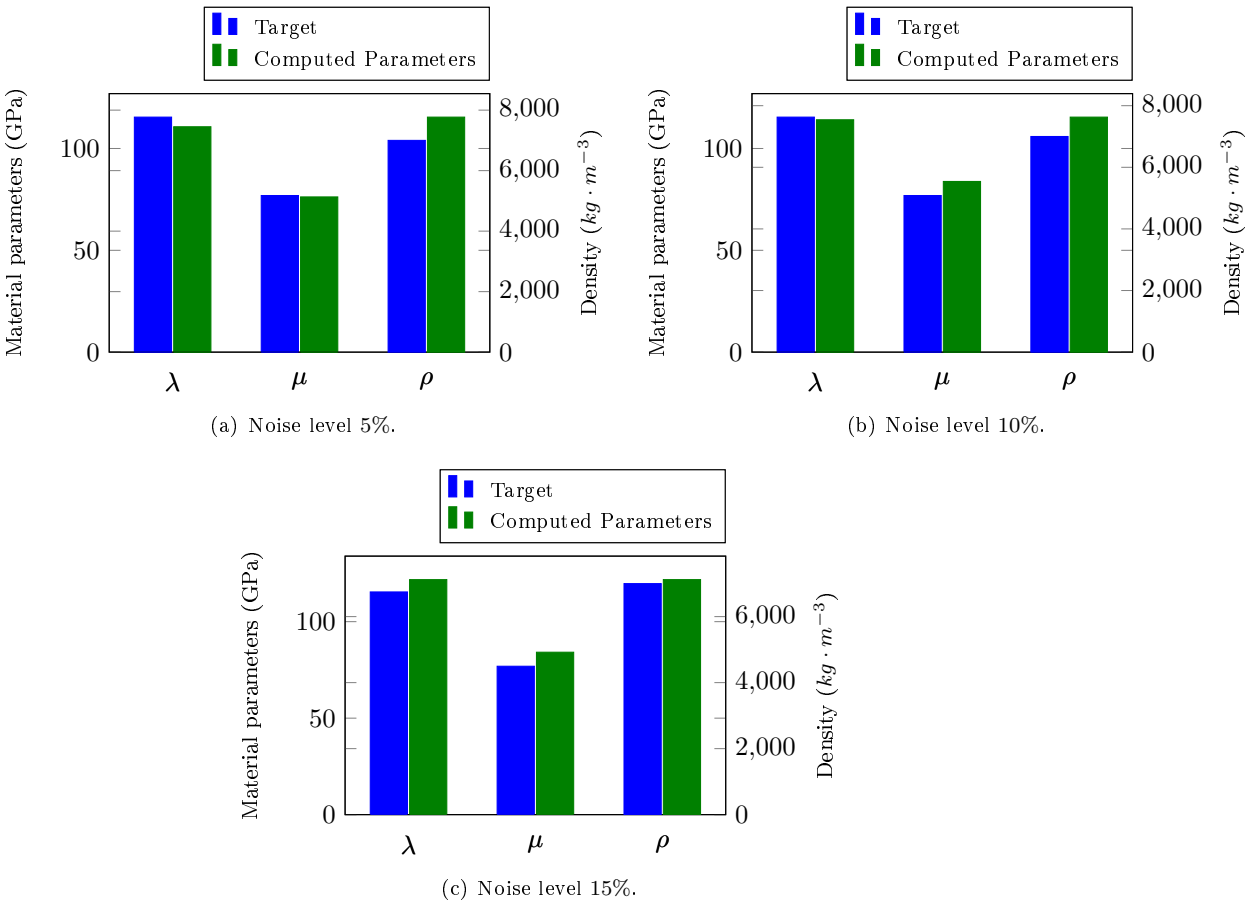

(a) Noise level 5%.

(b) Noise level 10%.

(c) Noise level 15%.

Figure 30: Accuracy level on the material parameter values in the case of the disk-shaped scatterer experiments. Sensitivity to the noise level in the measurements. $f = 71.61$kHz.

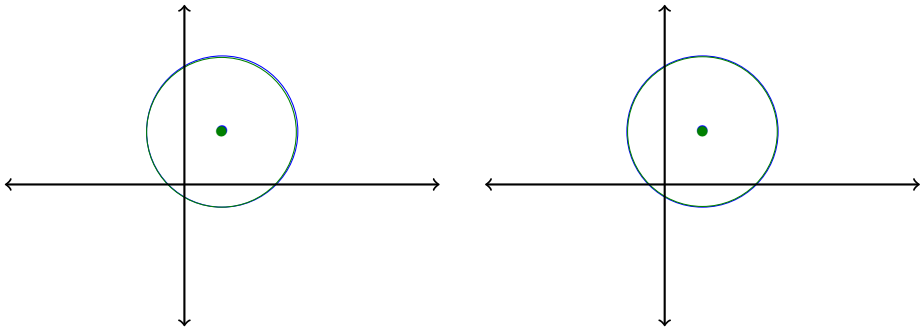

(*b*) Noise level 5%.

(*c*) Noise level 10%.

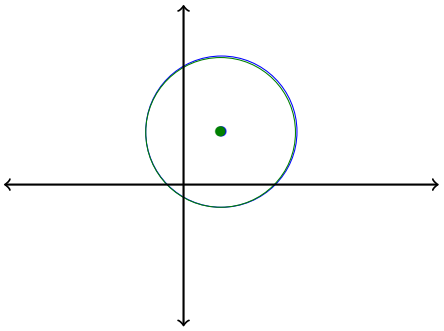

(*d*) Noise level 15%.

Figure 31: Accuracy level on the shape and location parameters in the case of the disk-shaped scatterer experiment. Sensitivity to the noise level in the measurements. $f = 71.61$kHz.

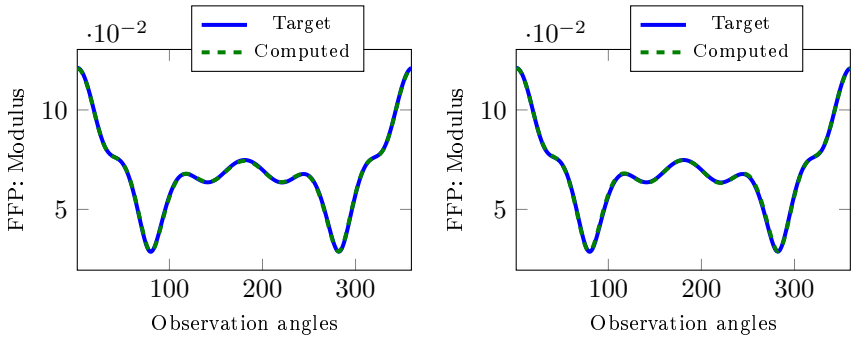

(a) Noise level 5%.

(b) Noise level 10%.

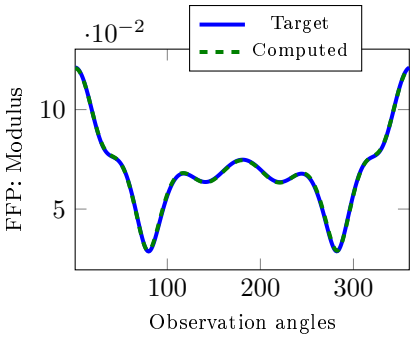

(c) Noise level 15%.

Figure 32: Accuracy level on the FFP intensity for the disk-shaped scatterer experiments: Target vs. Computed Values at convergence. Sensitivity to the noise level in the measurements. $f = 71.61$kHz.

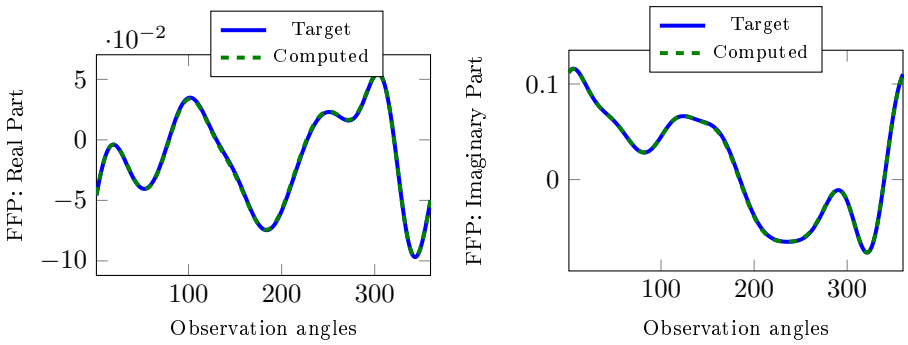

(a) Noise level 5%.

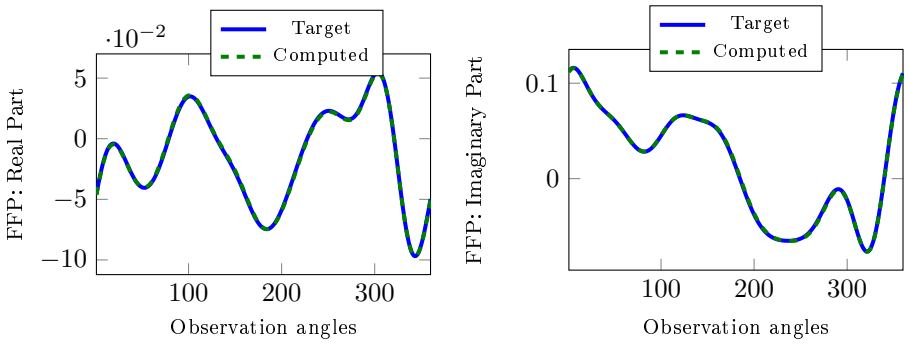

(b) Noise level 10%.

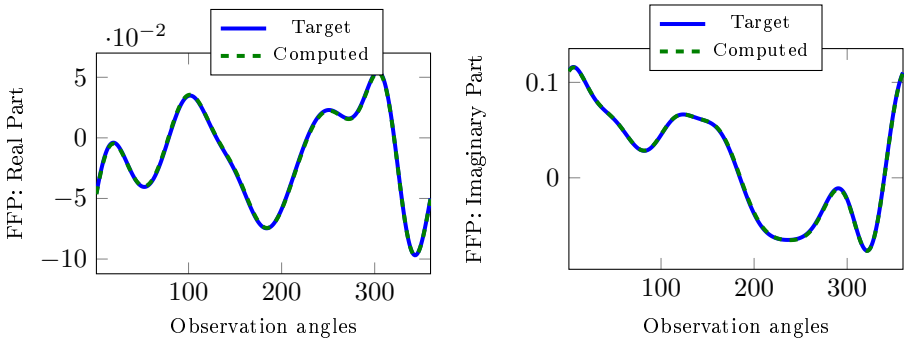

(c) Noise level 15%.

Figure 33: Accuracy level on the FFP for the disk-shaped scatterer experiments: Target vs. Computed Values at convergence. Sensitivity to the noise level in the measurements. $f = 71.61$kHz.

difference is that we add to the measured FFP depicted in Fig. 11 white noise of three different levels: 5%, 10%, and 15%, as depicted in Figs. 34-35. The results reported in Figs. 36-40 and Table 10, clearly indicate that, similarly to the disk-shaped scatterer, the proposed computational strategy exhibits high performance efficiency. Indeed, we observe that:

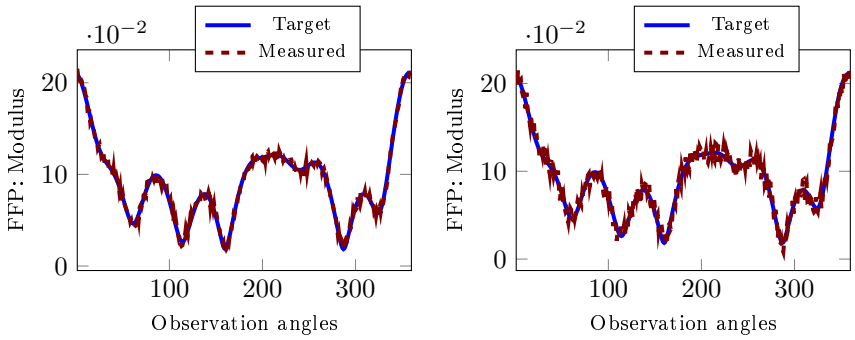

(a) Noise level 5%.

(b) Noise level 10%.

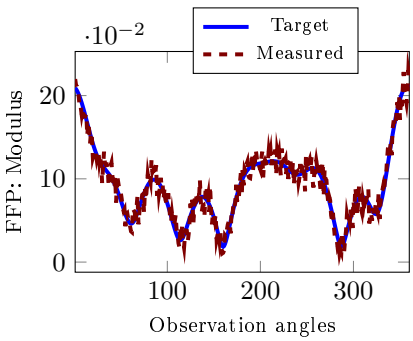

(c) Noise level 15%.

Figure 34: FFP intensity for the octagon-shaped scatterer experiments: Target vs. Measured. $f = 55.7$kHz and noise levels in the measurement: $5\%, 10\%, 15\%$.

- For all three noise levels, the proposed computational methodology is initiated outside the pre-asymptotic convergence region. Indeed, Fig. 36 shows that the initial residuals on the FFP intensity (resp. the full FFP), for all noise levels, exceed 80% (resp. 120%).
- Fig. 36 and Table 10 demonstrate the convergence of the proposed method. Indeed, the relative residuals reach the noise levels in -at most- 18 iterations for each stage, regardless of the noise level.
- The sought-after parameters of the scatterer are retrieved with a high accuracy level, as reported in Table 10 and depicted in Figs. 37-38.
- Figs. 39-40 also illustrate the high performance accuracy and robustness to the noise of the proposed method. These two figures show that the computed FFP at convergence is in agreement with the Target one.

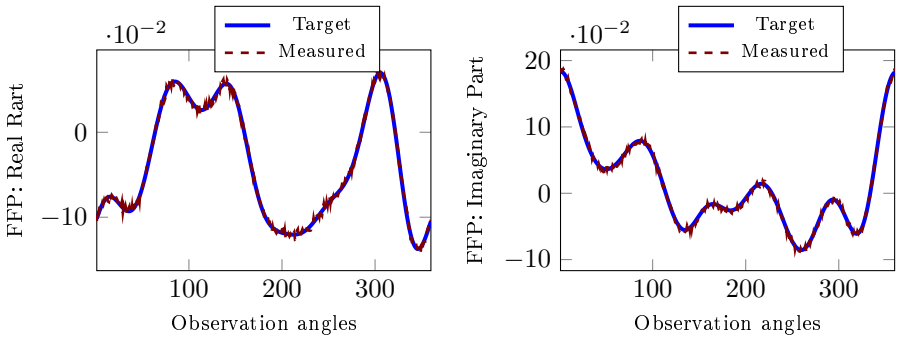

(a) Noise level 5%.

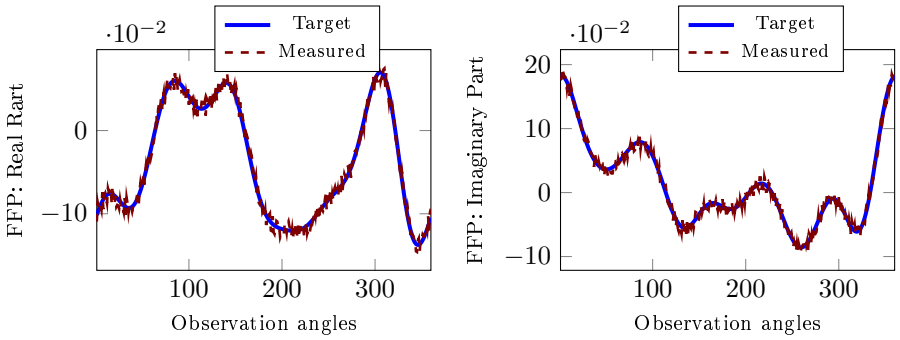

(b) Noise level 10%.

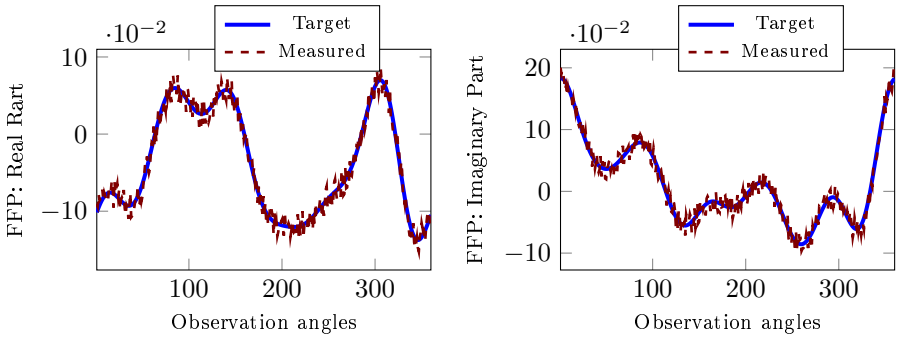

(c) Noise level 15%.

Figure 35: Full FFP for the octagon-shaped scatterer experiments: Target vs. Measured. $f = 55.7$kHz and noise levels in the measurements: $5\%, 10\%, 15\%$.

Noise level	Relative Residual (%)		Relative Error (%)			
	Intensity	Field	Shape	Lamé	Density	Location
0%	1.02	1.88	1.02	2.61	0.47	1.53
5%	4.95	5.53	2.05	4.53	0.96	1.75
10%	10.98	12.77	4.64	9.14	11.58	3.87
15%	15.2	15.36	5.86	11.81	18.69	5.01

Table 10: Final relative residual and relative errors for the octogonal-shaped scatterer experiments, sensitivity to the noise level in the measurements. $f = 55.7$kHz.

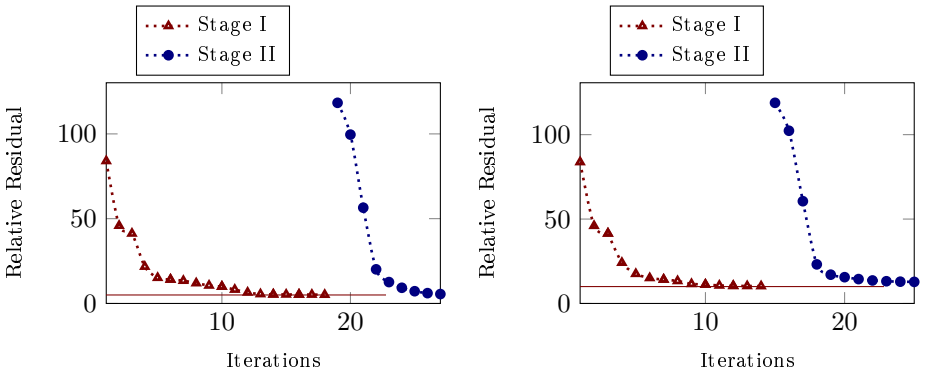

(a) Noise level 5%.

(b) Noise level 10%.

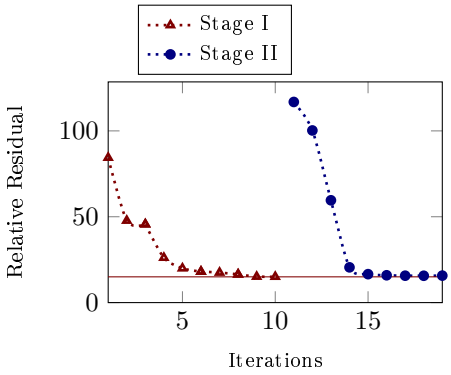

(c) Noise level 15%.

Figure 36: Convergence history for the octogonal-shaped scatterer experiments. Sensitivity to the noise level in the measurements. $f = 55.7$kHz.

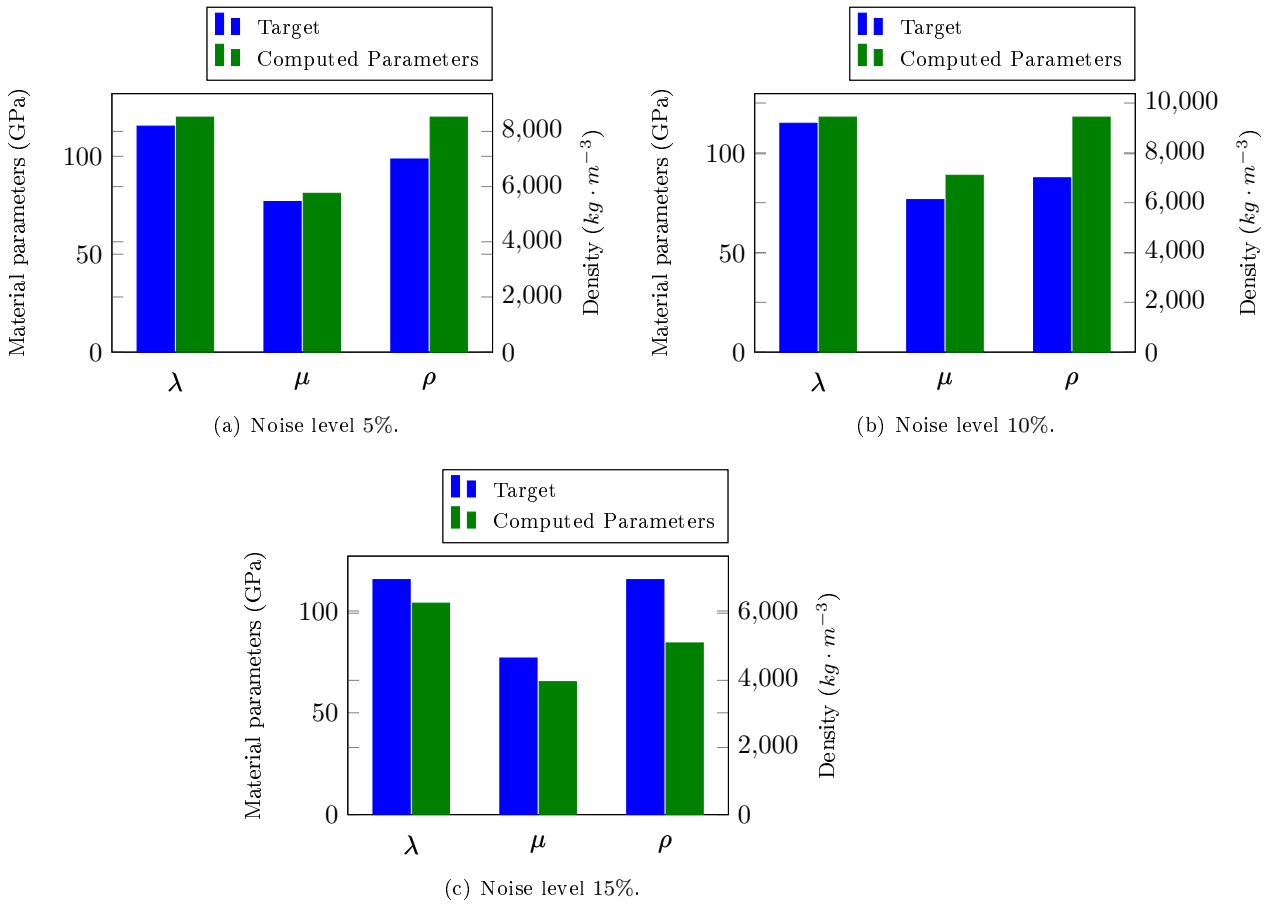

(a) Noise level 5%.

(b) Noise level 10%.

(c) Noise level 15%.

Figure 37: Accuracy level on the material parameter values in the case of octagon-shaped scatterer experiments. Sensitivity to the noise level in the measurements. $f = 55.7$kHz.

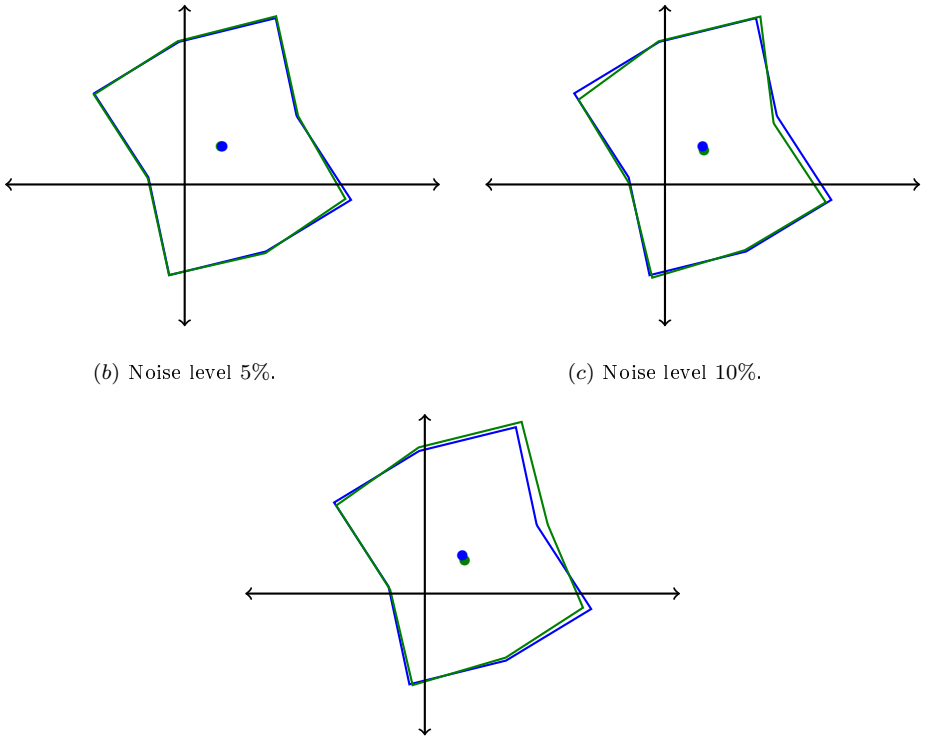

(*b*) Noise level 5%.

(*c*) Noise level 10%.

(*d*) Noise level 15%.

Figure 38: Accuracy level on the shape and location parameters in the case of the octagon-shaped scatterer experiment. Sensitivity to the noise level in the measurements. $f = 55.7$kHz.

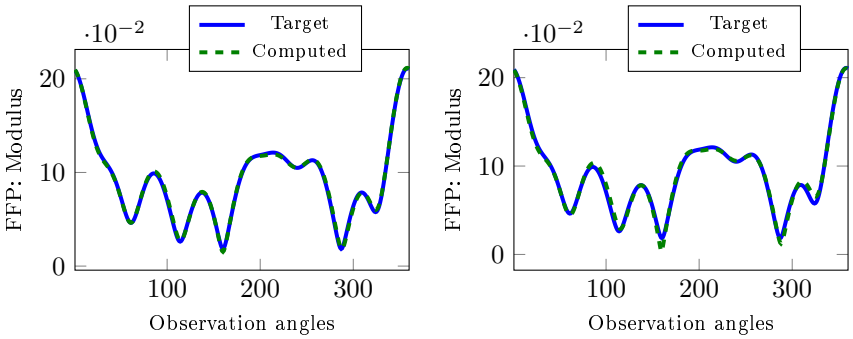

(a) Noise level 5%.

(b) Noise level 10%.

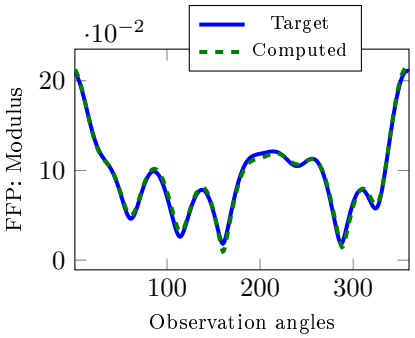

(c) Noise level 15%.

Figure 39: Accuracy level on the FFP intensity for the octagon-shaped scatterer experiments: Target vs. Computed Values at convergence. Sensitivity to the noise level in the measurements. $f = 55.7$kHz.

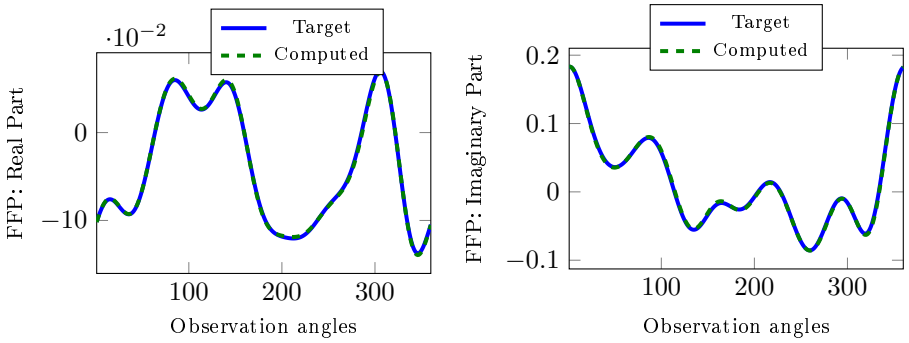

(a) Noise level 5%.

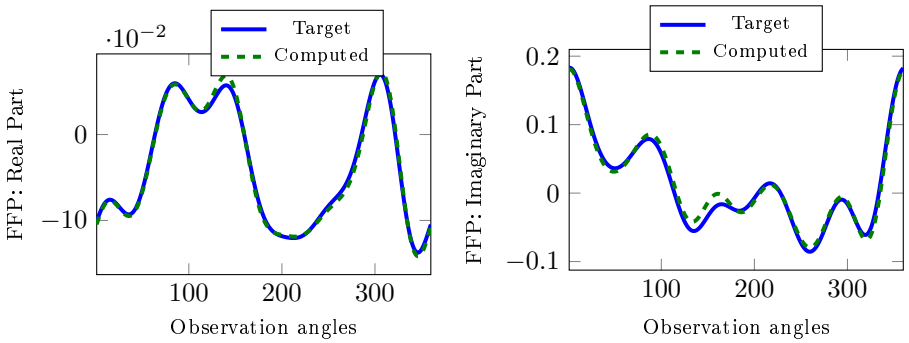

(b) Noise level 10%.

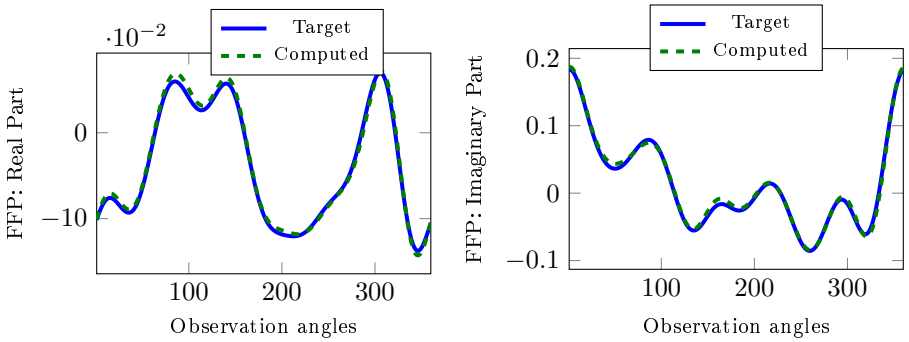

(c) Noise level 15%.

Figure 40: Accuracy level on the FFP for the octagon-shaped scatterer experiments: Target vs. Computed Values at convergence. Sensitivity to the noise level in the measurements. $f = 55.7$kHz.

5.3 Recovery of the parameters with multiple-frequency measurements

We present here numerical results demonstrating that using FFP measurements corresponding to more than one frequency significantly improves the performance accuracy of the proposed algorithm. The improvement in the accuracy is particularly noticeable when retrieving the material parameters with highly noisy data. We consider the thirteen parameters inverse problem introduced in section 5.1.3. Specifically, the goal is to recover the parameter's values of the mockup submarine made of aluminum depicted in Fig. 19(a). These values are reported in Table 6 and Fig. 20. We initiate the algorithm from the same circular-shaped domain introduced in section 5.1.3 (see Fig. 19(b), Fig. 20 and Table 6). We employed in this numerical experiments two sets of FFP measurements. We first apply the algorithm using FFP data corresponding to an angular frequency $\omega_1 = 0.35$, i.e., $f_1 = 55.7$kHz, the frequency regime used in section 5.1.3. When Stage II of the algorithm is completed, i.e., at convergence or stagnation, we re-apply the algorithm starting from the obtained final domain configuration, but this time using FFP measurements corresponding to a higher frequency regime $\omega_2 = 1$ ($f_2 = 159.15$kHz). Note that both sets of FFP measurements are tainted with white noise of level ranging from 0% to 15% (see Figs. 44, 45, 46). The results of these numerical experiments are reported in Table 11 and Figs. 44-49. These results suggest the following remarks:

- Similarly to all previous experiments, the algorithm, in this case, is initiated outside the pre-asymptotic convergence region. Indeed, the initial configuration, a circular-shaped domain, differs significantly from the target mockup submarine, as indicated in Fig. 19 and Table 6.

- Fig. 47 reveals that the proposed algorithm has already converged and reached the noise level when using the FFP measurements corresponding to the first frequency f_1 (see Figs. 44-46). On the one hand, the accuracy on the shape parameters at convergence is quite satisfactory, as reported in Table 11 and depicted in Fig. 49. On the other hand, the recovery of the material parameters and location is less accurate but still acceptable, as reported in Table 11. Given the reasonable quality of the reconstruction, one may even consider to stop the experiment at this step.

- Using FFP measurements for higher frequency ($f_2 = 159.15$kHz) and re-initiating the algorithm from the computed configuration with the FFP data corresponding to the lower frequency ($f_1 = 55.7$kHz) enables to retrieve all the parameters with a quite remarkable accuracy, particularly for highly noisy measurements. Indeed, the accuracy on the material parameters is improved by a factor two to over an order of magnitude, depending on the noise level. Moreover, accuracy on the location is significantly improved (up to a factor 5 in the case of 15% noise level), as reported in Table 11 and Fig. 49.

6 Bibliography

References

[1] Patrick R Amestoy, Iain S Duff, Jean-Yves L'Excellent, and Jacko Koster. A fully asynchronous multifrontal solver using distributed dynamic scheduling. SIAM Journal on Matrix Analysis and Applications, 23(1):15–41, 2001.

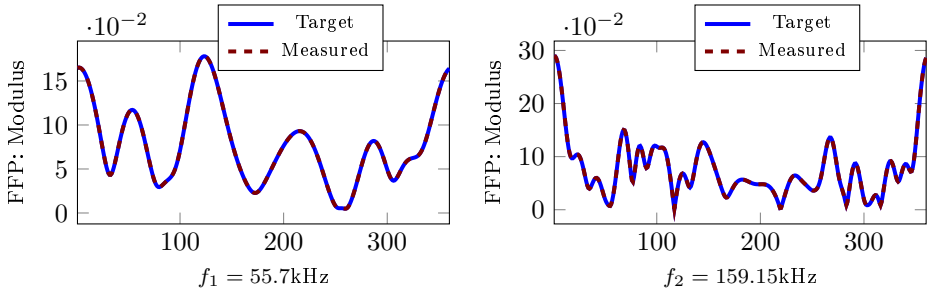

(a) Noise level 0%.

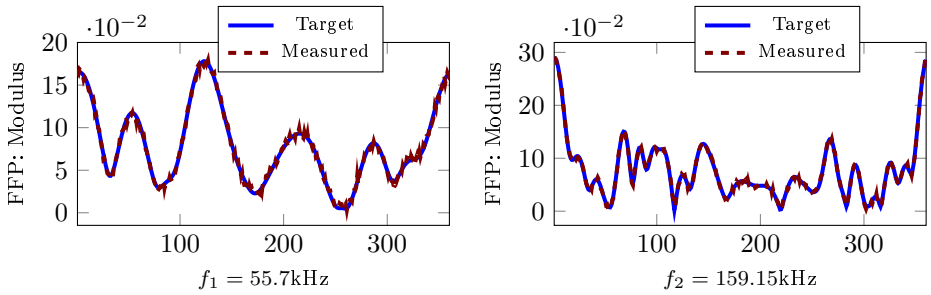

(b) Noise level 5%.

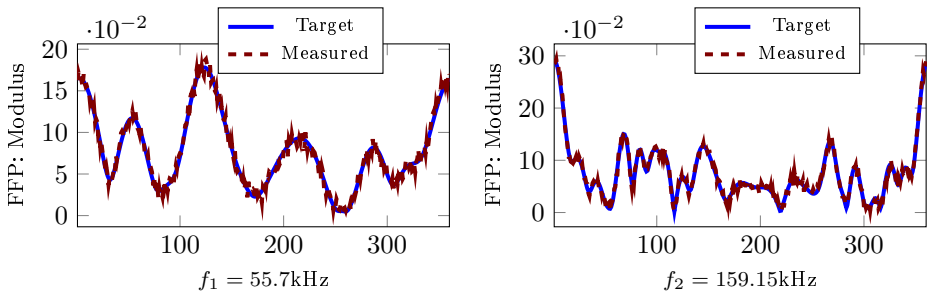

(c) Noise level 10%.

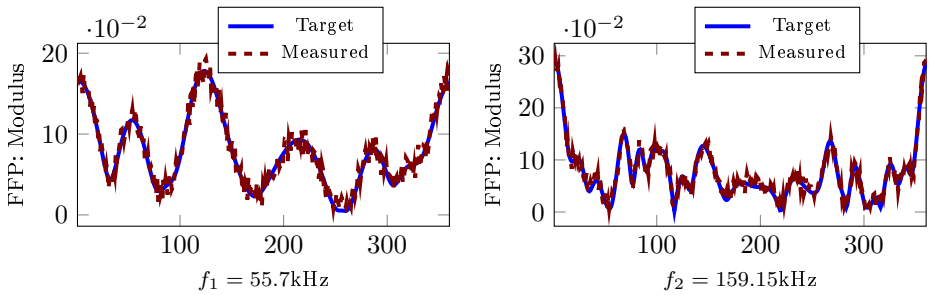

(d) Noise level 15%.

Figure 41: FFP intensity for the mockup submarine scatterer experiments: Target vs. Measured. $f = 55.7$kHz and noise levels in the measurements: $0\%, 5\%, 10\%, 15\%$.

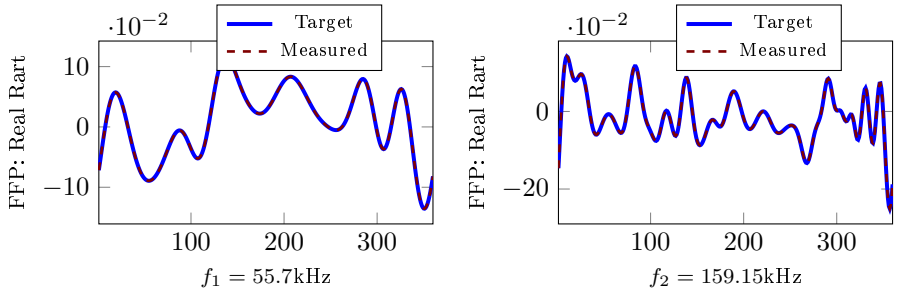

(a) Noise level 0%.

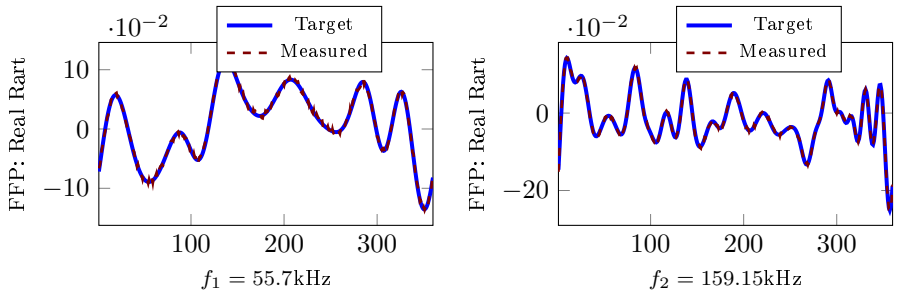

(b) Noise level 5%.

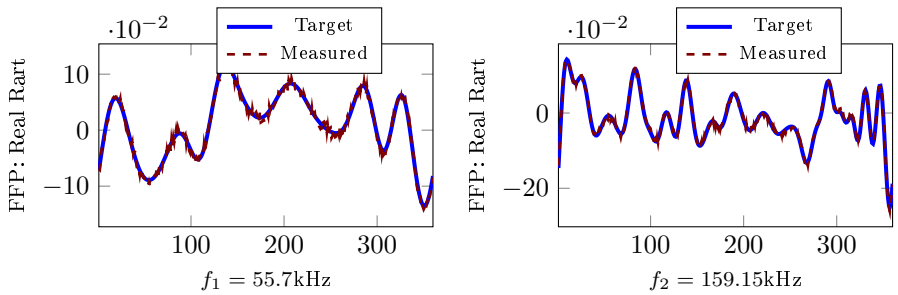

(c) Noise level 10%.

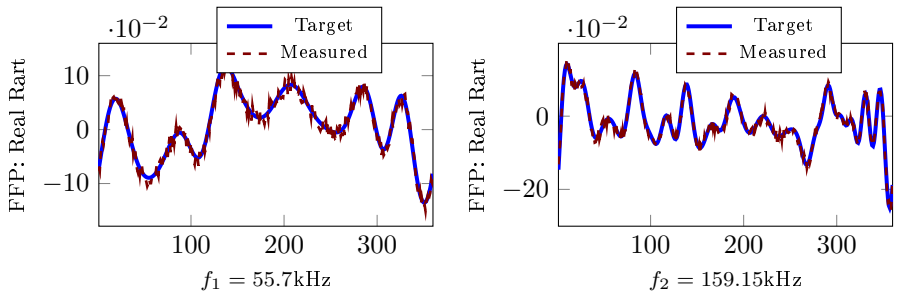

(d) Noise level 15%.

Figure 42: Real FFP for the mockup submarine scatterer experiments: Target vs. Measured. $f = 55.7$kHz and noise levels in the measurements: $0\%, 5\%, 10\%, 15\%$.

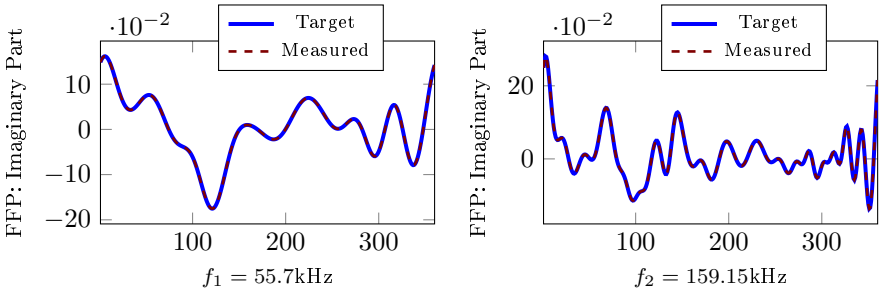

(a) Noise level 0%.

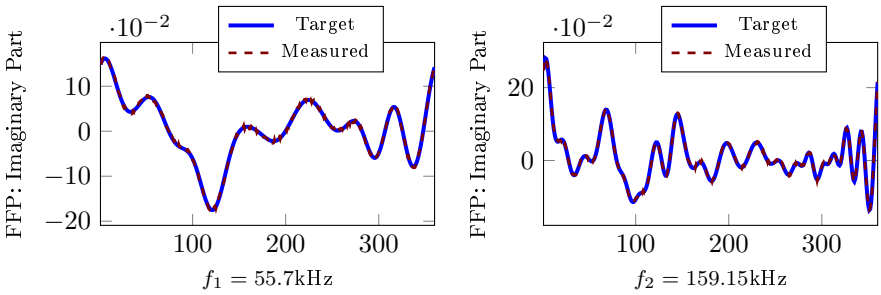

(b) Noise level 5%.

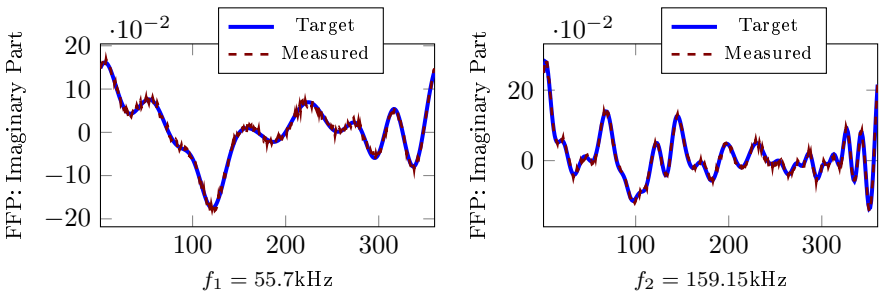

(c) Noise level 10%.

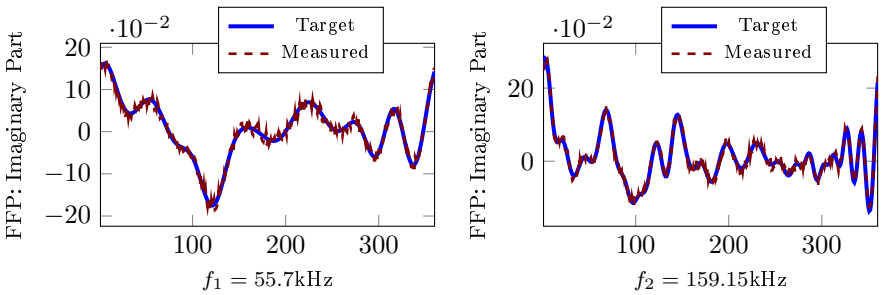

(d) Noise level 15%.

Figure 43: Imaginary FFP for the mockup submarine scatterer experiments: Target vs. Measured. $f = 55.7$kHz and noise levels in the measurements: $0\%, 5\%, 10\%, 15\%$.

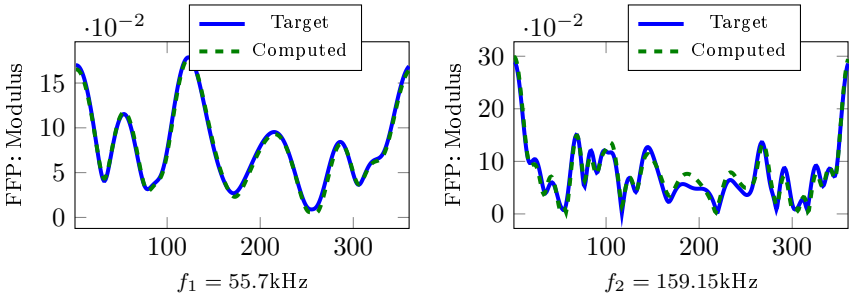

(a) Noise level 0%.

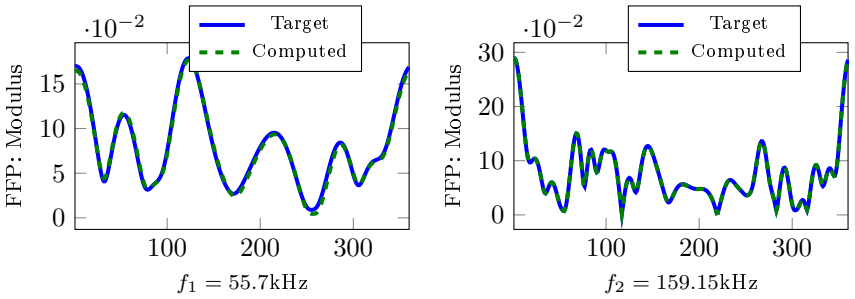

(b) Noise level 5%.

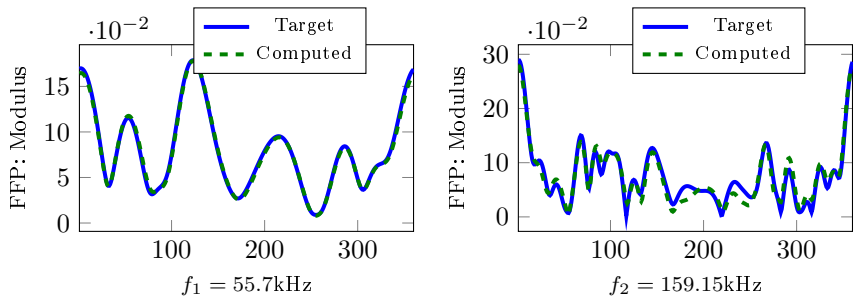

(c) Noise level 10%.

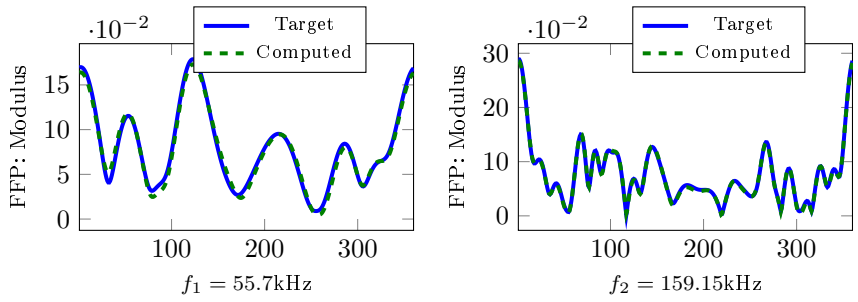

(d) Noise level 15%.

Figure 44: Accuracy on the FFP intensity for the mockup submarine scatterer experiments: Target vs. Computed Values at stagnation. Sensitivity to the noise level in the measurements. Case of a two frequencies reconstruction: $f_1 = 55.7$kHz and $f_2 = 159.15$kHz.

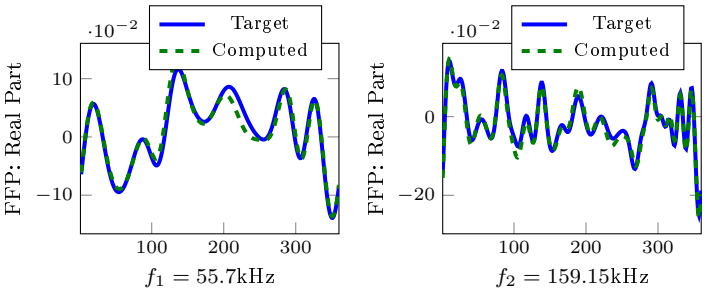

(a) Noise level 0%.

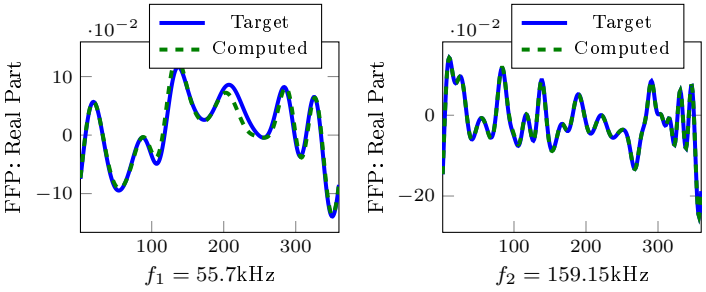

(b) Noise level 5%.

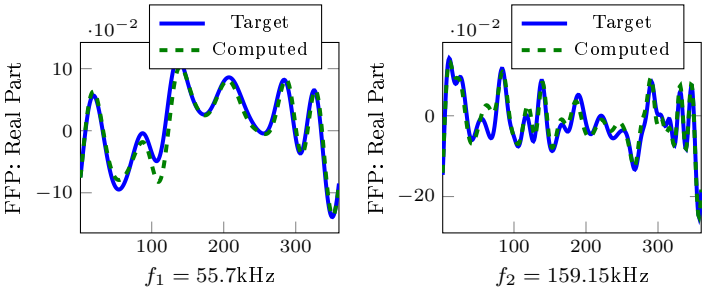

(c) Noise level 10%.

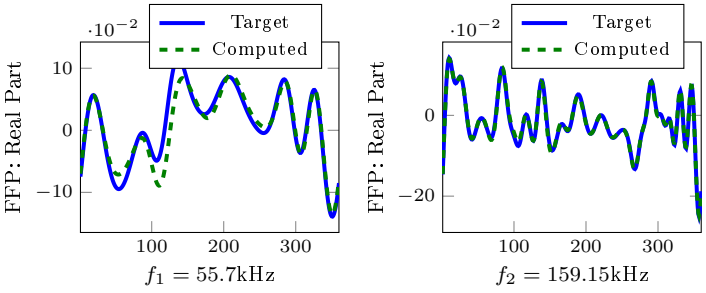

(d) Noise level 15%.

Figure 45: Accuracy on the real FFP for the mockup submarine scatterer experiments: Target vs. Computed Values at stagnation. Sensitivity to the noise level in the measurements. Case of a two frequencies reconstruction: $f_1 = 55.7$kHz and $f_2 = 159.15$kHz.

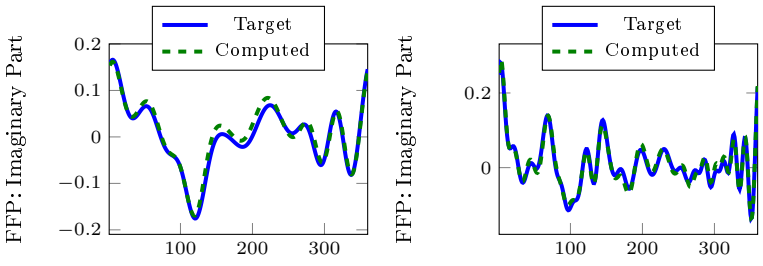

$f_1 = 55.7\text{kHz}$ $f_2 = 159.15\text{kHz}$

(a) Noise level 0%.

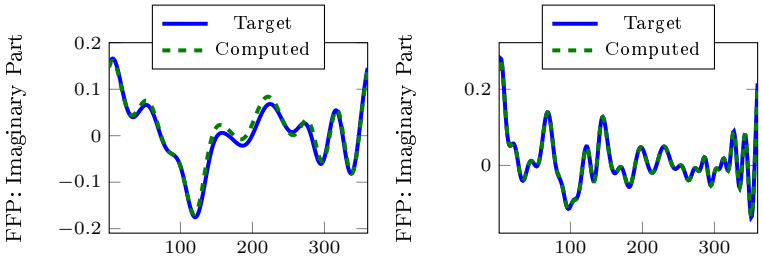

$f_1 = 55.7\text{kHz}$ $f_2 = 159.15\text{kHz}$

(b) Noise level 5%.

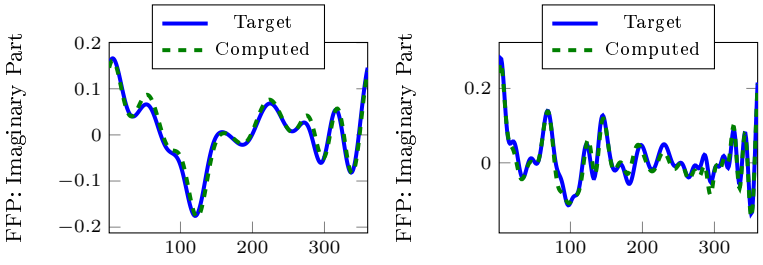

$f_1 = 55.7\text{kHz}$ $f_2 = 159.15\text{kHz}$

(c) Noise level 10%.

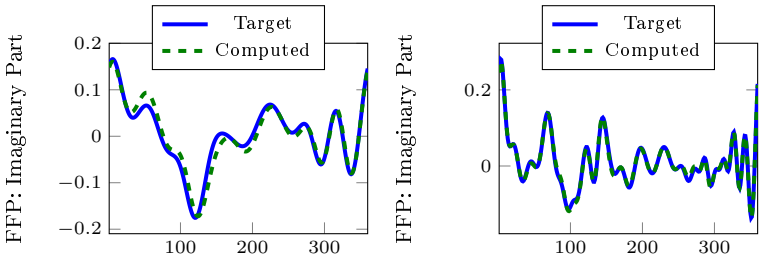

$f_1 = 55.7\text{kHz}$ $f_2 = 159.15\text{kHz}$

(d) Noise level 15%.

Figure 46: Accuracy on the imaginary FFP for the mockup submarine scatterer experiments: Target vs. Computed Values at stagnation. Sensitivity to the noise level in the measurements. Case of a two frequencies reconstruction: $f_1 = 55.7\text{kHz}$ and $f_2 = 159.15\text{kHz}$.

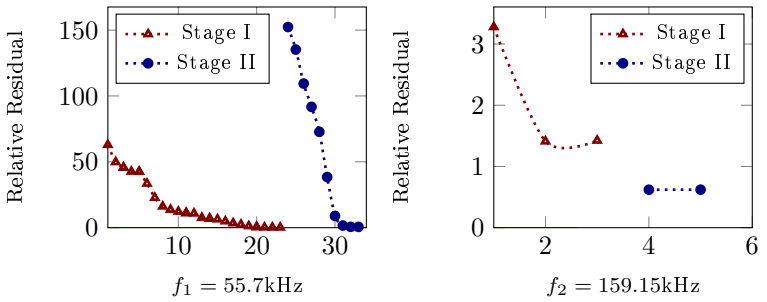

(a) Noise level 0%

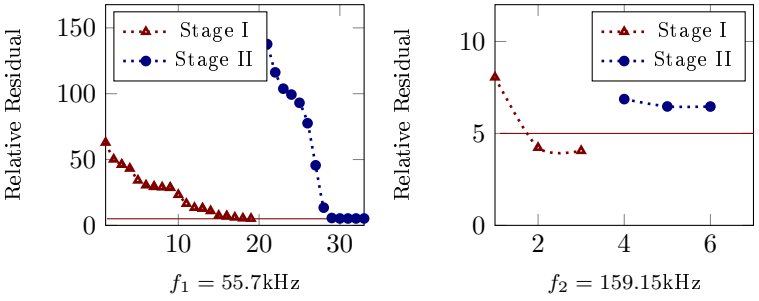

(b) Noise level 5%

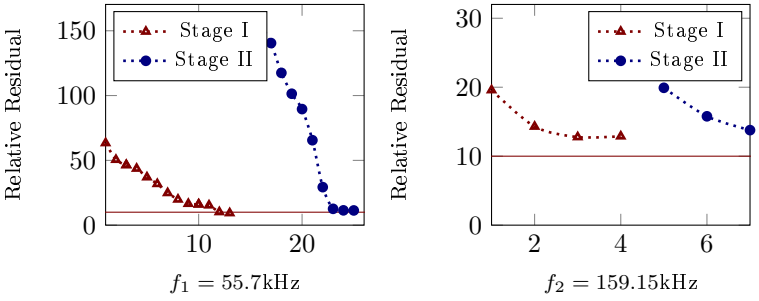

(c) Noise level 10%

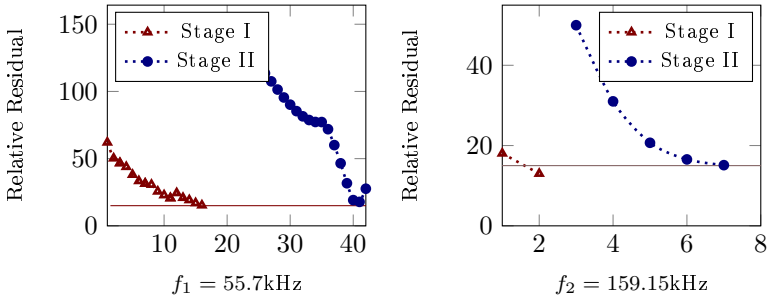

(d) Noise level 15%

Figure 47: Convergence history for the mockup submarine scatterer experiments. Sensitivity to the noise level in the measurements. Case of a two frequencies reconstruction: $f_1 = 55.7$kHz and $f_2 = 159.15$kHz.

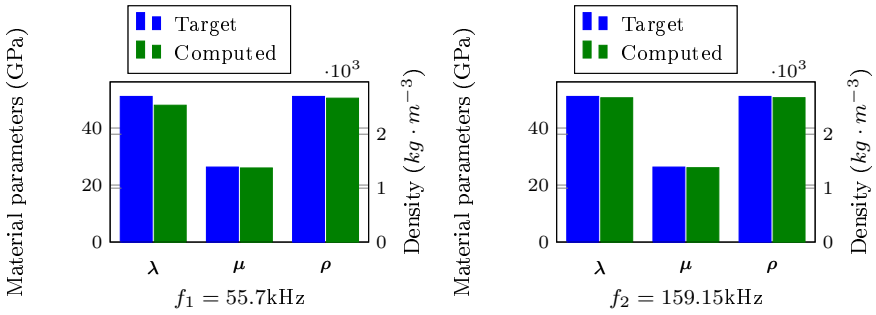

(a) Noise level 0%.

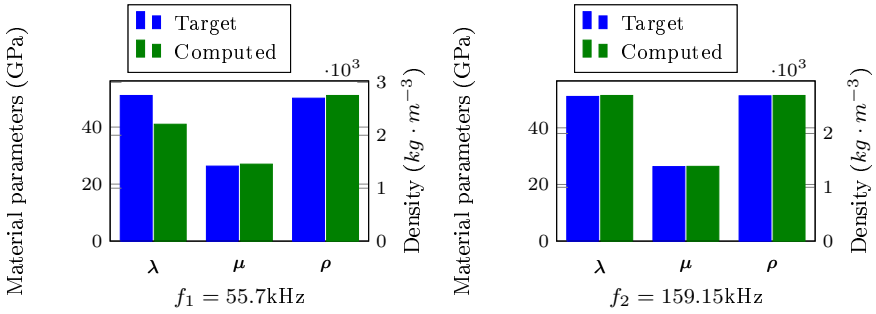

(b) Noise level 5%.

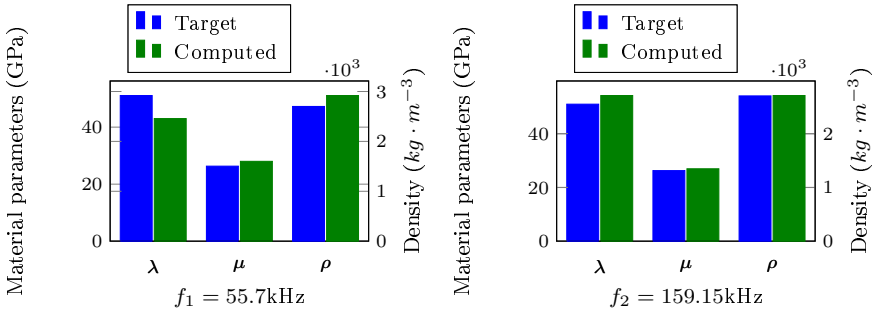

(c) Noise level 10%.

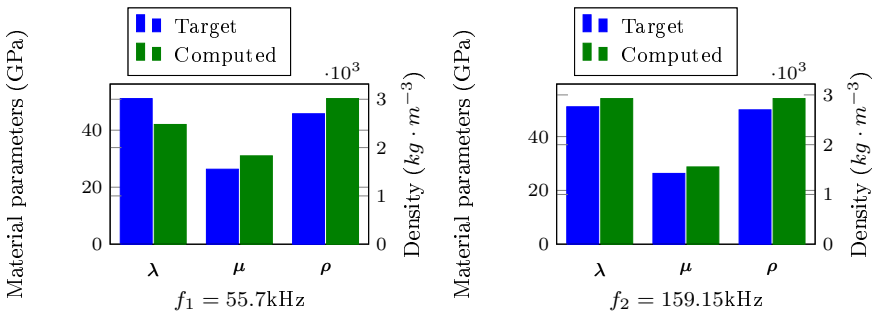

(d) Noise level 15%.

Figure 48: Accuracy level on the material parameter values for the mockup submarine scatterer experiments. Sensitivity to the noise level in the measurements. Case of a two frequencies reconstruction: $f_1 = 55.7$kHz and $f_2 = 159.15$kHz.

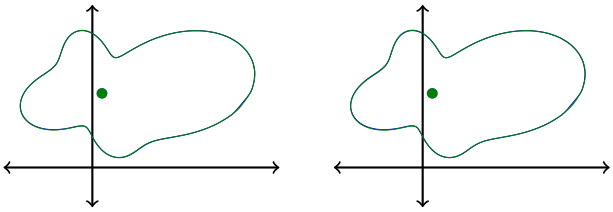

$f_1 = 55.7\text{kHz}$ $f_2 = 159.15\text{kHz}$

(a) Noise level 0%.

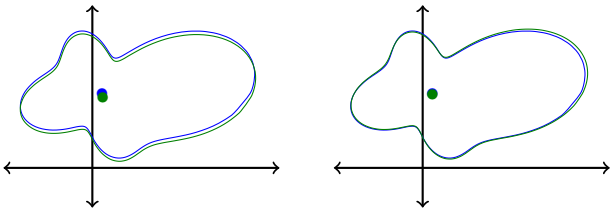

$f_1 = 55.7\text{kHz}$ $f_2 = 159.15\text{kHz}$

(b) Noise level 5%.

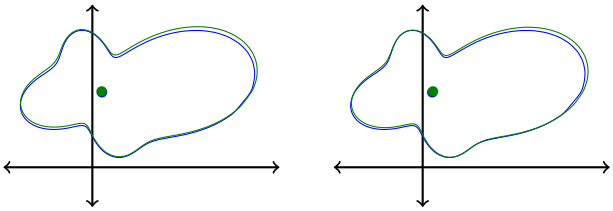

$f_1 = 55.7\text{kHz}$ $f_2 = 159.15\text{kHz}$

(c) Noise level 10%.

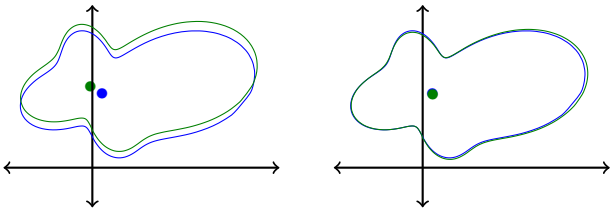

$f_1 = 55.7\text{kHz}$ $f_2 = 159.15\text{kHz}$

(d) Noise level 15%.

Figure 49: Accuracy level on the shape and location parameters' values for the mockup submarine scatterer experiments. Sensitivity to the noise level in the measurements. Case of a two frequencies reconstruction: $f_1 = 55.7\text{kHz}$ and $f_2 = 159.15\text{kHz}$.

Frequency (kHz)	Noise level	Relative Residual (%)		Relative Error (%)			
		Intensity	Field	Shape	Lamé	Density	Location
$f_1 = 55.7$	**0**%	0.17	0.57	0.43	4.96	1.15	0.12
	5%	5.12	5.23	1.60	17.55	4.95	0.53
	10%	9.30	11.34	3.79	14.19	14.33	2.29
	15%	15.29	17.82	2.34	17.15	11.36	4.75
$f_2 = 159.15$	**0**%	1.42	1.09	0.50	0.90	0.84	0.21
	5%	4.05	6.46	0.53	0.89	0.90	0.21
	10%	12.76	13.05	3.75	2.52	0.68	1.66
	15%	13.01	14.62	2.33	6.74	8.37	0.91

Table 11: Relative Residual and Relative error for the mockup submarine scatterer experiments. Sensitivity to the noise level in the measurements. Case of a two frequencies reconstruction: $f_1 = 55.7$kHz and $f_2 = 159.15$kHz.

[2] Patrick R Amestoy, Abdou Guermouche, Jean-Yves L'Excellent, and Stéphane Pralet. Hybrid scheduling for the parallel solution of linear systems. Parallel computing, 32(2):136–156, 2006.

[3] Habib Ammari, Ekaterina Iakovleva, and Dominique Lesselier. A MUSIC algorithm for locating small inclusions buried in a half-space from the scattering amplitude at a fixed frequency. Multiscale Modeling & Simulation, 3(3):597–628, 2005.

[4] TS Angell, David Colton, and Andreas Kirsch. The three dimensional inverse scattering problem for acoustic waves. Journal of Differential Equations, 46(1):46–58, 1982.

[5] Xavier Antoine, Helene Barucq, and Abderrahmane Bendali. Bayliss–turkel-like radiation conditions on surfaces of arbitrary shape. Journal of Mathematical Analysis and Applications, 229(1):184–211, 1999.

[6] Izar Azpiroz. Contribution to the Numerical Reconstruction in Inverse Elasto-Acoustic Scattering. PhD thesis, Université de Pau et des Pays de l'Adour, 2018.

[7] Izar Azpiroz, Hélène Barucq, Rabia Djellouli, and Ha Pham. Characterization of partial derivatives with respect to material parameters in a fluid-solid interaction problem. Journal of Mathematical Analysis and Applications, 465(2):903–927, 2018.

[8] Hélène Barucq, Julien Diaz, and Véronique Duprat. Long-term stable acoustic absorbing boundary conditions for regular-shaped surfaces. Technical report, RR-8203,INRIA hal-00776058, 2013.

[9] Helene Barucq, Rabia Djellouli, and Elodie Estecahandy. Efficient DG-like formulation equipped with curved boundary edges for solving elasto-acoustic scattering problems. International Journal for Numerical Methods in Engineering, 98(10):747–780, 2014.

[10] Hélène Barucq, Rabia Djellouli, and Elodie Estecahandy. On the existence and the uniqueness of the solution of a fluid–structure interaction scattering problem. Journal of Mathematical Analysis and applications, 412(2):571–588, 2014.

[11] Helene Barucq, Rabia Djellouli, and Elodie Estecahandy. Fréchet differentiability of the elasto-acoustic scattered field with respect to Lipschitz domains. Mathematical Methods in the Applied Sciences, 40(2):404–414, 2017.

[12] Helene Barucq, Rabia Djellouli, Elodie Estecahandy, and Mohand Moussaoui. Mathematical determination of the Fréchet derivative with respect to the domain for a fluid-structure scattering problem: Case of polygonal-shaped domains. SIAM Journal on Mathematical Analysis, 50(1):1010–1036, 2018.

[13] Hélène Barucq, Florian Faucher, and Ha Pham. Localization of small obstacles from back-scattered data at limited incident angles with full-waveform inversion. Journal of Computational Physics, 370:1–24, 2018.

[14] Alvin Bayliss and Eli Turkel. Radiation boundary conditions for wave-like equations. Communications on Pure and applied Mathematics, 33(6):707–725, 1980.

[15] G Beylkin and R Burridge. Linearized inverse scattering problems in acoustics and elasticity. Wave motion, 12(1):15–52, 1990.

[16] Biondo L Biondi. 3D seismic imaging. Society of Exploration Geophysicists, 2006.

[17] Laurent Bourgeois, Nicolas Chaulet, and Houssem Haddar. On simultaneous identification of the shape and generalized impedance boundary condition in obstacle scattering. SIAM Journal on Scientific Computing, 34(3):A1824–A1848, 2012.

[18] John J Bowman, Thomas B Senior, and Piergiorgio L Uslenghi. Electromagnetic and acoustic scattering by simple shapes. Technical report, Michigan Univ. Ann Arbor Radiation Lab., 1970.

[19] Fioralba Cakoni and David Colton. Qualitative methods in inverse scattering theory: An introduction. Springer Science & Business Media, 2005.

[20] Fioralba Cakoni and David Colton. A qualitative approach to inverse scattering theory. Springer, 2014.

[21] Fioralba Cakoni, David Colton, and Peter Monk. Qualitative methods in inverse electromagnetic scattering theory: Inverse scattering for anisotropic media. IEEE Antennas and Propagation Magazine, 59(5):24–33, 2017.

[22] Fioralba Cakoni and Isaac Harris. The factorization method for a defective region in an anisotropic material. Inverse Problems, 31(2):025002, 2015.

[23] Zhiming Chen and Xinming Wu. An adaptive uniaxial perfectly matched layer method for time-harmonic scattering problems. Numer. Math. Theor. Meth. Appl, 1:113–137, 2008.

[24] Philippe G Ciarlet. The finite element method for elliptic problems, volume 40. SIAM, 2002.

[25] David Colton, Joe Coyle, and Peter Monk. Recent developments in inverse acoustic scattering theory. Siam Review, 42(3):369–414, 2000.

[26] David Colton and Andreas Kirsch. A simple method for solving inverse scattering problems in the resonance region. Inverse problems, 12(4):383, 1996.

[27] David Colton and Rainer Kress. Inverse acoustic and electromagnetic scattering theory, volume 93. Springer Science & Business Media, 2012.

[28] F.A. Dahlen and Jeroen Tromp. Theoretical global seismology. Princeton university press, 1998.

[29] Rabia Djellouli. Inverse acoustic problems. In Frédéric Magoulès, editor, Computational methods for acoustics problems, pages 263–294. Saxe-Coburg Publications,, Stirlingshire (UK), 2008.

[30] Johannes Elschner, George C Hsiao, and Andreas Rathsfeld. An optimization method in inverse acoustic scattering by an elastic obstacle. SIAM Journal on Applied Mathematics, 70(1):168–187, 2009.

[31] Heinz Werner Engl, Martin Hanke, and Andreas Neubauer. Regularization of inverse problems, volume 375. Springer Science & Business Media, 1996.

[32] Charbel Farhat, Radek Tezaur, and Rabia Djellouli. On the solution of three-dimensional inverse obstacle acoustic scattering problems by a regularized Newton method. Inverse problems, 18(5):1229, 2002.

[33] Roohallah Fazli and Mansor Nakhkash. An analytical approach to estimate the number of small scatterers in 2D inverse scattering problems. Inverse Problems, 28(7):075012, 2012.

[34] Gonzalo R Feijoo, Manish Malhotra, Assad A Oberai, and Peter M Pinsky. Shape sensitivity calculations for exterior acoustics problems. Engineering computations, 18(3/4):376–393, 2001.

[35] Andreas Fichtner. Full seismic waveform modelling and inversion. Springer Science & Business Media, 2010.

[36] Sergei Farshatovich Gilyazov and NL Gol'dman. Regularization of ill-posed problems by iteration methods, volume 499. Springer Science & Business Media, 2013.

[37] Roland Griesmaier and Christian Schmiedecke. A multifrequency MUSIC algorithm for locating small inhomogeneities in inverse scattering. Inverse Problems, 33(3):035015, 2017.

[38] Jacques Hadamard. Lectures on Cauchy's problem in linear partial differential equations. Courier Corporation, 2014.

[39] Per Christian Hansen and Dianne Prost O'Leary. The use of the L-curve in the regularization of discrete ill-posed problems. SIAM Journal on Scientific Computing, 14(6):1487–1503, 1993.

[40] Thierry Hargé. Valeurs propres d'un corps élastique. Comptes rendus de l'Académie des sciences. Série 1, Mathématique, 311(13):857–859, 1990.

[41] Simon Hubmer, Ekaterina Sherina, Andreas Neubauer, and Otmar Scherzer. Lamé parameter estimation from static displacement field measurements in the framework of nonlinear inverse problems. SIAM Journal on Imaging Sciences, 11(2):1268–1293, 2018.

[42] Olha Ivanyshyn. Shape reconstruction of acoustic obstacles from the modulus of the far field pattern. Inverse Problems and Imaging, 1(4):609, 2007.

[43] Olha Ivanyshyn and Rainer Kress. Identification of sound-soft 3D obstacles from phaseless data. Inverse Problems and Imaging, 4(1):131–149, 2010.

[44] Olha Ivanyshyn and Rainer Kress. Inverse scattering for surface impedance from phase-less far field data. Journal of Computational Physics, 230(9):3443–3452, 2011.

[45] Miguel C Junger and David Feit. Sound, structures, and their interaction, volume 225. MIT press Cambridge, MA, 1986.

[46] Michael V Klibanov. Phaseless inverse scattering problems in three dimensions. SIAM Journal on Applied Mathematics, 74(2):392–410, 2014.

[47] Michael V Klibanov and Vladimir G Romanov. Reconstruction procedures for two inverse scattering problems without the phase information. SIAM Journal on Applied Mathematics, 76(1):178–196, 2016.

[48] Rainer Kress. Newton method in inverse obstacle scattering inverse problem in engineering mechanics. In Proc. 2nd Int. Symp. Inv. Plobl., Paris, France, 1994, 1994.

[49] Rainer Kress. Integral equation methods in inverse obstacle scattering. Engineering analysis with boundary elements, 15(2):171–179, 1995.

[50] Rainer Kress and William Rundell. A quasi-Newton method in inverse obstacle scattering. Inverse Problems, 10(5):1145, 1994.

[51] Rainer Kress and William Rundell. Inverse obstacle scattering with modulus of the far field pattern as data. Inverse problems in medical imaging and nondestructive testing, pages 75–92, 1997.

[52] Gerhard Kristensson. Inverse problems for acoustic waves using the penalised likelihood method. Inverse Problems, 2(4):461, 1986.

[53] François Le Chevalier. Principles of radar and sonar signal processing. Artech House, 2002.

[54] Armin Lechleiter and John W Schlasche. Identifying Lamé parameters from time-dependent elastic wave measurements. Inverse Problems in Science and Engineering, 25(1):2–26, 2017.

[55] Lars Mönch. A Newton method for solving the inverse scattering problem for a sound-hard obstacle. Inverse Problems, 12(3):309, 1996.

[56] Peter Monk and Virginia Selgas. An inverse fluid–solid interaction problem. Inverse Problems & Imaging, 3(2):173–198, 2009.

[57] Peter Monk and Virginia Selgas. Near field sampling type methods for the inverse fluid–solid interaction problem. Inverse Problems & Imaging, 5(2):465–483, 2011.

[58] Vladimir Alekseevich Morozov. On the solution of functional equations by the method of regularization. In Doklady Akademii Nauk, volume 167, pages 510–512. Russian Academy of Sciences, 1966.

[59] Vladimir Alekseevich Morozov. Choice of parameter for the solution of functional equations by the regularization method. In Sov. Math. Doklady, volume 8, pages 1000–1003. Russian Academy of Sciences, 1967.

[60] C Pöppe, RD Murch, DGH Tan, DJN Wall, MV Klibanov, and J Malinsky. Newton-Kantorovich method applied to two-dimensional inverse scattering for an exterior Helmholtz problem. Inverse Problems, 5:1173, 1989.

[61] Haihua Qin and Xiaodong Liu. The linear sampling method for inhomogeneous medium and buried objects from far field measurements. Applied Numerical Mathematics, 105:82–95, 2016.

[62] André Roger. Newton-Kantorovitch algorithm applied to an electromagnetic inverse problem. IEEE Transactions on Antennas and Propagation, 29(2):232–238, 1981.

[63] CJ sound hard and Paul A Martin. Fluid–solid interaction: acoustic scattering by a smooth elastic obstacle. SIAM Journal on Applied Mathematics, 55(4):904–922, 1995.

[64] Albert Tarantola. Inverse problem theory and methods for model parameter estimation, volume 89. Siam, 2005.

[65] Andrei Nikolaevich Tikhonov. Regularization of incorrectly posed problems. In Soviet Mathematics Doklady, volume 4, pages 1624–1627, 1963.

[66] Andrei Nikolaevich Tikhonov and Vasili Ya Arsenin. Methods for solving ill-posed problems. John Wiley and Sons, Inc, 1977.

[67] W Tobocman. Inverse acoustic wave scattering in two dimensions from impenetrable targets. Inverse Problems, 5(6):1131, 1989.

[68] Jean Virieux and Stéphane Operto. An overview of full-waveform inversion in exploration geophysics. Geophysics, 74(6):WCC1–WCC26, 2009.

[69] Grace Wahba. Spline models for observational data, volume 59. Siam, 1990.

[70] Adriaan Walther. The ray and wave theory of lenses, volume 15. Cambridge University Press, 1995.

[71] SL Wang and YM Chen. An efficient numerical method for exterior and interior inverse problems of Helmholtz equation. Wave Motion, 13(4):387–399, 1991.

[72] James E Warner, Manuel I Diaz, Wilkins Aquino, and Marc Bonnet. Inverse material identification in coupled acoustic-structure interaction using a modified error in constitutive equation functional. Computational mechanics, 54(3):645–659, 2014.

[73] Bo Zhang and Haiwen Zhang. Recovering scattering obstacles by multi-frequency phaseless far-field data. Journal of Computational Physics, 345:58–73, 2017.

[74] Deyue Zhang and Yukun Guo. Uniqueness results on phaseless inverse acoustic scattering with a reference ball. Inverse Problems, 34(8):085002, 2018.

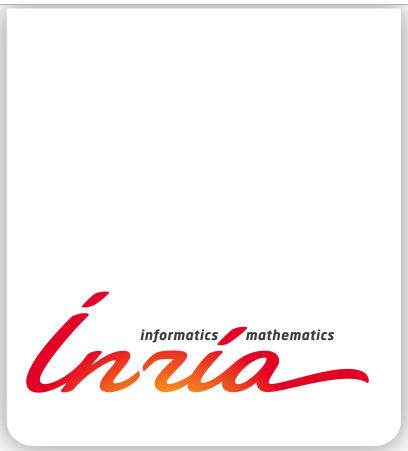

RESEARCH CENTRE
BORDEAUX – SUD-OUEST

200 avenue de la Vieille Tour
33405 Talence Cedex

Publisher
Inria
Domaine de Voluceau - Rocquencourt
BP 105 - 78153 Le Chesnay Cedex
inria.fr

ISSN 0249-6399